Tampere University

Tanmay Ram Godbole

EVALUATION OF COORDINATED DRONE SWARM OPERATION AS A SYNTHETIC APERTURE ANTENNA

A simulation-based study

Faculty of Information Technology and Communication Sciences
Master of Science Thesis
November 2019

ABSTRACT

Tanmay Ram Godbole: Evaluation of Coordinated Drone Swarm Operation as a Synthetic Aperture Antenna
Master of Science Thesis
Tampere University
Degree Programme in Information Technology
November 2019
Examiners: Asst. Prof. Sergey Andreev, Prof. Mikko Valkama
Supervisors: Dr. Alexander Pyattaev (YL-Verkot Oy), Asst. Prof. Sergey Andreev (Tampere University), Prof. Mikko Valkama(Tampere University)

This thesis investigates the performance of Synthetic Aperture Antennas formed by static formations of Unmanned Aerial Vehicle (UAV) swarms in terms of several selected parameters. Of equal importance is the methodology employed in the study, which makes use of a custom simulation platform. The developed simulation platform is unique in having the ability to concurrently model physics, robotics, and communications, while also handling antenna modeling. This makes it uniquely suited for the task of studying the trends arising from the complex processes involved in the operation of UAV swarms.

The formation shape, the use of inter-element spacing in formation control, the wavelength, and the wind strength are the various parameters whose effects are investigated. The results point to trade-offs made through the choice of one formation over another, while supporting the use of inter-element spacing in formation control. Additionally, wind is found to adversely affect performance, while larger wavelengths have the opposite effect.

The results obtained provide valuable insights into the operation of swarm-based Synthetic Aperture Antennas, which, while interesting in their own right, can also be utilized in the planning of operations making use of UAV swarms. Moreover, the study in this thesis demonstrates the validity and flexibility of application of the chosen methodology.

Keywords: UAV, Drone, Antenna, Synthetic Aperture Radar, Simulation

PREFACE

This thesis was written during my time as a Research Assistant at Tampere University. I would like to thank my examiners, Asst. Prof. Sergey Andreev and Prof. Mikko Valkama, for their involvement and support, both for this thesis and the larger project it has been a part of, without which none of this work would have been possible. I would especially like to thank my supervisor, teacher, and mentor, Dr. Alexander Pyattaev, for his guidance and encouragement which have proven invaluable for the work in this thesis and beyond.

The background for the work in this thesis has been a collaboration project between Tampere University and the University of Pennsylvania and Intel, and I would therefore like to thank everyone involved. Particular thanks go to Dr. Miguel Calvo-Fullana who has time and time again been generous with his help. Further thanks go to everyone else I met and worked with at Tampere University and YL-Verkot Oy. I am also grateful for the funding received from the aColor project under the Future Makers Funding Program 2017.

The support provided by my family has been indispensable for the successful completion of this thesis, and for this I would like to express my immense gratitude to my parents Ram and Smita Godbole, and my brother Tushar. Special thanks go to Kirsikka Nordström for her patience and support. Finally I would like to extend my thanks to those whom I may have inadvertently left out.

Tampere, 3rd November 2019

Tanmay Ram Godbole

CONTENTS

1 Introduction 1
2 Theoretical background and Methodology 3
2.1 Relevant Antenna Theory 3
2.1.1 Antenna Aperture 4
2.1.2 Synthetic Apertures 6
2.2 Miscellaneous Relevant Concepts 11
2.2.1 WiFi FTM Ranging 11
2.2.2 Drone Modeling 14
2.3 Methodology 15
2.3.1 Metrics and Parameters 15
2.3.2 Experiment Process 18
2.3.3 Data Analysis Procedure 19
2.3.4 Methodology Considerations 20
3 Experimental Setup 22
3.1 The Simulation Platform 22
3.1.1 Design Considerations 23
3.1.2 Overall Architecture 23
3.1.3 ROS + Gazebo Specifics 24
3.1.4 Network Simulator Specifics 27
3.1.5 NetWatcher Specifics 28
3.1.6 Postprocessing 34
3.2 Simulation Details 36
4 Results and analysis 40
4.1 Parameter Selection 40
4.2 Effects of Formation Shape and FTM Usage 47
4.3 Effects of Wavelength and Wind Strength 53
5 Conclusion 58
References 60

LIST OF FIGURES

2.1 A parabolic dish antenna . . . 3
2.2 Illustration of SAR operation with single platform . . . 7
2.3 Illustration of the Seasat satellite . . . 8
2.4 Illustration of multi-platform SAR . . . 10
2.5 WiFi FTM ranging mechanism . . . 12
2.6 Simulation pipeline . . . 19

3.1 Proposed simulation platform architecture . . . 24
3.2 Screenshots depicting UAVs in an ongoing simulation . . . 25
3.3 Ray casting: Interaction loss types . . . 26
3.4 Time synchronization mechanism . . . 29
3.5 TUN network operation . . . 31
3.6 A sample channel representation in ROS . . . 33
3.7 Examples of main lobe detection . . . 35
3.8 The different considered formations . . . 38

4.1 Formation performance vs. reliance on GPS . . . 40
4.2 Reflection coefficients for dipole antennas . . . 41
4.3 Radiation pattern for a $5m$ dipole antenna . . . 42
4.4 Structure and reflection coefficients for coil antennas . . . 42
4.5 A "star"-shaped antenna with a single loop and 28 segments . . . 43
4.6 A meander antenna with a single loop and 28 "meanders" . . . 43
4.7 Reflection coefficients for "star" antennas . . . 44
4.8 Reflection coefficients for meander antennas . . . 45
4.9 Radiation pattern for a meander antenna . . . 46
4.10 Radiation pattern for a $0.5m$ dipole antenna . . . 46
4.11 Antenna radiation pattern for various formations . . . 48
4.12 Results for formation variation with $f = 1$ . . . 49
4.13 Results for formation variation with $f = 0.6$ . . . 49
4.14 Results for formation variation with $f = 0.3$ . . . 50
4.15 Results for wavelength variation with $0N$ wind . . . 53
4.16 Results for wavelength variation with $2N$ wind . . . 54
4.17 Results for wavelength variation with $5N$ wind . . . 54
4.18 Radiation pattern comparison for an ideal and simulated antenna . . . 56

LIST OF SYMBOLS AND ABBREVIATIONS

AoA	Angle of Arrival
AP	Access Point
API	Application Programming Interface
BER	Bit Error Rate
CSI	Channel State Information
FTM	Fine Time Measurement
GPR	Ground Penetrating Radar
GPS	Global Positioning System
IMU	Inertial Measurement Unit
IoT	Internet of Things
IP	Internet Protocol, specifically IPv4 unless mentioned otherwise
JSON	JavaScript Object Notation
LIDAR	Light Detection and Ranging
LOS	Line-of-Sight
mmWave	Millimeter Wave
NLOS	Non-Line-of-Sight
OTH-Radar	Over-The-Horizon Radar
PDF	Probability Density Function
RMS	Root Mean Square
ROS	Robot Operating System
RSSI	Received Signal Strength Information
RTT	Round Trip Time
SAR	Synthetic Aperture Radar
ToF	Time of Flight
TUN	Virtual IP Interface (Network TUNnel)
UAV	Unmanned Aerial Vehicle
UWB	Ultra-Wideband
WSN	Wireless Sensor Networks

1 INTRODUCTION

Unmanned Aerial Vehicles (UAVs) are becoming increasingly more widespread, with numerous new applications making use of them having come up in recent years [29]. One of these applications is that of radar, as shown by the work in [17]. In these, as in more traditional communications-based applications, there is an operational constraint that is straight away faced: the antenna sizes that can be readily mounted on UAVs are highly limited. This severely limits the potency (in terms of gain) of the antenna mounted on a UAV, while also making it unsuitable for operating at larger wavelengths.

As an example of an application requiring larger wavelengths, Ground Penetrating Radar (GPR) has been known to be implemented on space based platforms [31] and manned aircraft [15]. These mobile platforms allow for safely surveying hazardous or inaccessible environments while also speeding up the process, which paves the way for an equally capable but lower cost solution making use of smaller unmanned rotor-based UAVs. Unsurprisingly, there have been various efforts which aim to develop a UAV mounted GPR system [2, 13, 20, 60], demonstrating the ubiquity and relevance of UAV-based systems.

The size constraints faced when making use of UAV-mounted systems operating at larger wavelengths immediately bring to mind the idea of making use of synthetic apertures, possibly enhancing performance through the use of a swarm, and indeed there has been previous work dealing with this exact topic [6, 7, 10]. The work in this thesis continues in the same vein, but aims to provide more realism while also allowing for greater flexibility in the examination of various systems.

A unique simulation platform has been newly developed which allows for the realistic simulation of the operation of UAVs. This simulator is central to the developed methodology, which leverages it to obtain valuable insights into the operation of an Synthetic Aperture Antenna formed by a swarm of UAVs. Specifically, the performance of the synthetic antenna is examined in terms of a few different selected operational parameters; these are the formation shape, type of formation control, wind strength, and operating wavelength.

In this sense, the work in this thesis is limited to simulation studies; no real-life measurements are taken. Parameter variation attempts to identify a suitably well performing configuration, i.e. the tested values and especially formations are by no means exhaustive; the selection of a truly optimal working configuration depends on the priorities for a given use case and is not a problem tackled in this work. Additionally, the effects of the input parameters are examined in a way which allows for a qualitative understanding;

precise numerical relationships are out of the scope of this work.

There are previous works dealing with the formation of antennas through the use of highly mobile UAV swarms [6, 7, 10]. However, compared to these efforts, the methodology adopted in this work allows for added realism – in the physics, robotics, and communications aspects. The newly available insights into the operation of Synthetic Aperture Antennas help to optimize various operational choices for any given use case, with the use of a simulator enabling rapid prototyping and testing.

For example, a planned GPR mission could test the performance of a particular antenna configuration by simulating a world with targets to be imaged at the estimated depth. In that sense, although the selected scenarios in this work primarily explore the effects of the selected parameters (i.e. formation shape, formation control parameters, wavelength, wind), they additionally serve as an example application of the developed methodology.

In line with the description so far, the work in this thesis aims to provide insights into a few different operational and environmental parameters that affect the performance of swarm-based Synthetic Aperture Antennas. The first of these is the formation shape built by the UAVs, since antenna theory suggests that it is one of the most fundamental choices to be made. Also examined are a few different types of formation control algorithms, varying in their usage of inter-element distance estimations to improve positioning accuracy.

Next, the effect of changing the operational wavelength is considered, especially in comparison to an intuitive expectation of its effects. Lastly, the variation in performance under different wind strengths is examined, as this is an important real-world factor that affects virtually every outdoor operation of drone swarms. It is also especially important in this case since position/orientation deviations together are arguably the single most important consideration for the performance of any given formation, and these deviations can be expected to be directly affected by wind.

The study of the above mentioned effects is possible due to the selected methodology, for which it additionally serves as a representative example. The methodology itself can be considered one of the main contributions of this work, alongside the conclusions drawn from the study of the selected factors.

Beyond this introduction, the content in this thesis starts off in Chapter 2 with a description of the theoretical background that underpins the topics dealt with in this thesis. The same chapter further contains an account of the methodology used in this work. The next chapter (Chapter 3) contains details of the simulation platform that has been leveraged in this work, followed by a description of the scenarios that were studied through simulation.

This is followed by Chapter 4 which presents the results obtained from the simulations, along with their analysis. In closing, Chapter 5 contains the conclusions that are drawn from the carried out study, with a focus on whether the objectives that have been set forth are met. Additionally, possible avenues for future work are suggested based on the experiences from the work in this thesis.

2 THEORETICAL BACKGROUND AND METHODOLOGY

Before diving into the details of the work, it is important to first have a sufficient understanding of certain underlying concepts. It is also equally important to understand the motivation behind the effort, and the reasoning behind decisions affecting the implementation of the study.

The aim of this chapter is to answer these questions, and consequently this chapter consists of two main parts: the theoretical background (which contains the sufficient minimum knowledge that provides a context for the work) and the methodology (which describes the procedure of, and the design choices behind, the central effort of this thesis).

2.1 Relevant Antenna Theory

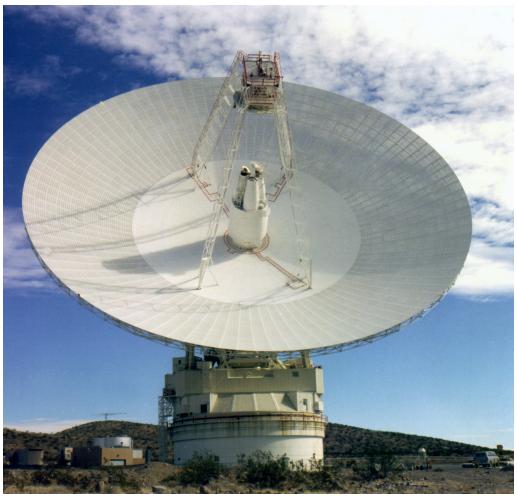

Figure 2.1. *A parabolic dish antenna, one of the most widely recognizable types of antenna (Image credit: NASA[1])*

This section presents certain selected theoretical aspects of the operation of antennas. There is a description of the idea of the aperture of an antenna, along with its relation with other fundamental properties of antennas. The need for large antenna apertures is thereby stressed. Following this, the concept of synthetic apertures is introduced, with

[1] `https://www.nasa.gov/sites/default/files/images/515900main_DSN_big.jpg`

a special focus on its relevance and implementation alternatives. All these concepts together provide a foundation for the subsequent discussion.

2.1.1 Antenna Aperture

The aperture of an antenna is a measure of the efficiency of an antenna receiving power from an electromagnetic wave [22]. Alternatively, it can be considered to be the "effective area", i.e. the area that contributes to actual received power for a given power flow per unit area at the antenna. Specifically,

$$A_{eff} = \frac{P_r}{P_0},$$

or equivalently,

$$P_r = A_{eff} \cdot P_0,$$

where A_{eff} is the effective area (i.e. antenna aperture), P_r is the power available at the output terminals of a receiving antenna, and P_0 is the power per unit area of the incident field. This indicates that an antenna with larger aperture requires lesser power to produce an equally strong received signal. Conversely, while transmitting, a larger aperture antenna requires less power to be applied to produce the same signal.

The antenna aperture is in turn related to the physical size of the antenna through the antenna efficiency. Specifically:

$$A_{eff} = e_a \cdot A_{phy},$$

where A_{eff} is the effective area (i.e. antenna aperture), A_{phy} is the physical aperture, and e_a is the antenna efficiency. This implies that efficiency remaining constant, physically larger antennas have larger antenna apertures, giving the power benefits mentioned above.

The aperture of an antenna directly affects certain antenna properties [3, 49, 62, 63, 68] as follows:

- Gain:

  The gain of an antenna is the ratio of the power produced by an antenna to the power produced by an isotropic antenna. The gain of an antenna varies by direction, and the maximum gain is related to the aperture in the following manner:

  $$G = \frac{4\pi}{\lambda^2} \cdot A_{eff},$$

  where A_{eff} is the antenna aperture, λ is the wavelength, and G is the antenna gain. This follows from the fact that the aperture of an isotropic antenna is $\frac{\lambda^2}{4\pi}$. The maximum gain of an antenna is therefore directly proportional to antenna aperture.

- Directivity:

  The directivity of an antenna is the ratio of the power density in a given direction compared to an isotropic antenna with the same transmit power. Directivity is related to gain as

  $$G(\theta, \phi) = e_{cd} \cdot D(\theta, \phi),$$

  where $G(\theta, \phi)$ and $D(\theta, \phi)$ are gain and directivity for a given direction, and e_{cd} is the antenna's radiation efficiency. This makes the maximum directivity of an antenna proportional to antenna aperture, through its relation to maximum gain. A high peak directivity value implies that the antenna transmits strongly in a given direction as compared to others.

- Beamwidth/angular resolution:

  The beamwidth of an antenna is the angle between the half-power points of the main lobe of the antenna radiation pattern. A smaller beamwidth thus means that the directivity decreases rapidly when moving away from the main transmission direction. For a fixed wavelength, an increase in the antenna aperture reduces the beamwidth.

- Antenna bandwidth:

  The bandwidth of an antenna is the range of frequencies over which it is designed to operate. Outside of these frequencies, the radiation efficiency is reduced, resulting in a loss of directive gain. Operating frequency of an antenna in turn affects its efficiency. To maintain good efficiency, the physical antenna length is required to be comparable to the wavelength of the corresponding wave. Specifically, antenna lengths below $\frac{\lambda}{2}$ see low efficiency. Antennas operating at lower frequencies therefore need to have larger apertures.

The relation of the above-mentioned properties with antenna aperture is important because it places constraints on the aperture for real-world use cases. For example, high antenna gain is important to virtually all communication and radar applications, as it helps to ease the constraints of the link budget, providing advantages such as better range, higher tolerance to interference, lower requirement for transmit power, etc. Similarly, directivity is critical to applications such as radar, imaging (for example in ground-based radio telescopes), and beamforming in general [67]. An antenna's beamwidth directly affects the angular resolution available, which is a critical consideration in tasks like radar and imaging. Additionally, applications such as Wireless Sensor Networks (WSN) (which is an important facet of the Internet of Things (IoT)), and certain radars operate at low frequencies which imply relatively large wavelengths. For example, GPR (which is one potential target application of the configurations considered in this work) usually operates at 10MHz+, i.e. wavelengths up to $30m$. Similarly, Over-The-Horizon Radar (OTH-Radar) operates at 3MHz+, resulting in a wavelength as large as $100m$.

These requirements, i.e. high gain, directivity, and large wavelengths, all in turn bring up

the need to have a large antenna aperture, a requirement that is readily fulfilled by having a physically large antenna. Unfortunately, the antenna sizes needed to satisfy these requirements can prove to be challenging to install and operate in certain environments. For example, in the case of the German TerraSAR-X radar satellite, it has been mentioned that to achieve the desired resolution of one meter on the ground with existing operational requirements, an antenna of at least 15 kilometers [64] in length would be needed.

This has been one of the motivations for the use of antenna arrays [24], which provide the benefits of a large antenna aperture through the combination of numerous smaller antenna units, connected in a predetermined manner. The phases of the signals from each individual antenna unit are carefully adjusted so that the waves combine constructively in a desired direction (i.e. giving higher gain and directivity), while cancelling each other out in others. Another benefit is that having the antennas rigidly physically connected enables analog addition of the signals received in each individual element, resulting in greater sensitivity.

While this is satisfactory for static and permanent installations, having large rigidly connected antenna arrays is either impractical or impossible for applications which are by nature mobile and highly dynamic. Examples of these are satellites in space [42] or mobile UAVs [46]. These cases are therefore prime candidates for the application of Synthetic Aperture Antennas. Continuing the example of the mentioned German TerraSAR-X radar satellite, synthetic aperture techniques are used to achieve the desired resolution with a physical antenna merely 5 meters in length, as opposed to the 15 kilometers that would otherwise be needed (i.e. an aperture equivalent to $15km$ is synthesized using a mobile $5m$ antenna).

2.1.2 Synthetic Apertures

Synthetic aperture techniques were developed to overcome the operational limitations of large antennas or antenna arrays in environments such as space [43], or when mounted on mobile platforms such as UAVs. Le Vine succinctly describes the working of this technique in [42] (for the context of radio imaging of an environment, i.e. Synthetic Aperture Radar (SAR)), "In aperture synthesis, the coherent product (correlation) of the signal from pairs of antennas is measured at different antenna-pair spacings (baselines). The product at each baseline yields a sample point in the Fourier transform of the brightness temperature map of the scene, and the scene itself is reconstructed by inverting the sampled transform". Further details can be found in [41, 44, 65].

The most common way that this is implemented is now described. A single physical antenna, mounted on a mobile platform (moving along a predetermined path) gathers signals from different positions at different times. These signals are stored based on the position at which they were obtained. On combination (as previously mentioned), and with additional processing, the resulting signal is equivalent to one that would have been

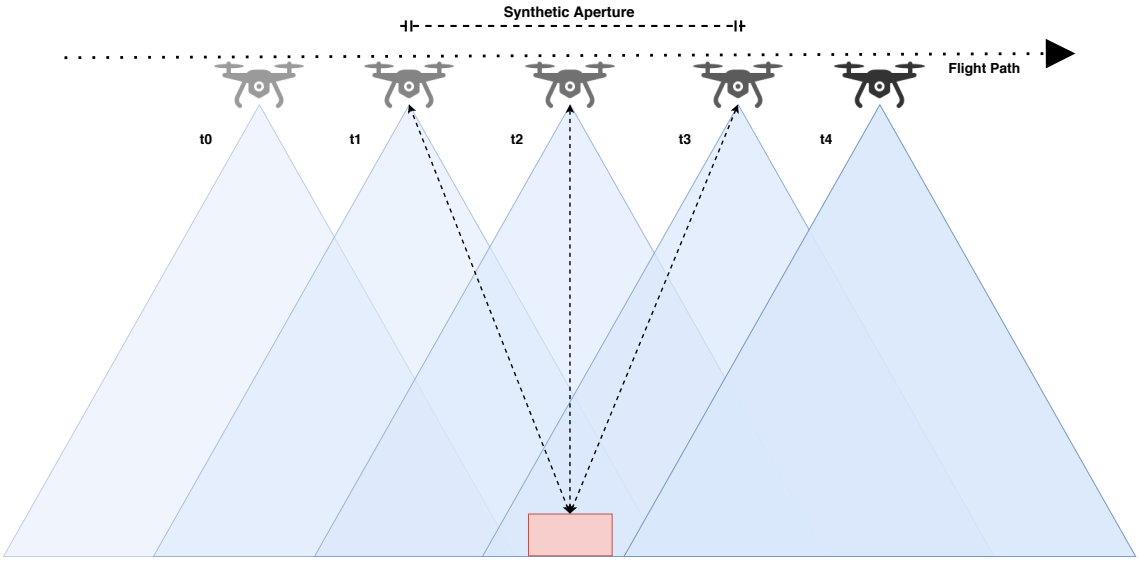

Figure 2.2. *Illustration of SAR operation with single platform*

obtained from an antenna with a much larger aperture (specifically an aperture as large as the traveled path).

This mechanism, although seemingly different from a phased antenna array, operates on much of the same principles. A phased antenna array consists of precisely positioned (in one or more dimensions) individual antenna elements. A controlled phase shift is then applied to signals to/from each antenna, resulting in the overall antenna "pointing" in a chosen direction (while having higher gain, and equivalent aperture, than any of the constituent elements). In Synthetic Aperture Antennas, each signal snapshot contains similar phase shifts (which come from factors like the position/velocity each snapshot was obtained at), which can be adjusted in further processing of the signals. Hence it can be understood that Synthetic Aperture Antennas recreate the effects of a phased array through processing of the signals, just as an antenna array does through physical geometry.

It should be noted that the operation of a Synthetic Aperture Antenna is not limited to a single mobile platform. As evident from numerous examples [6, 7, 10, 18, 38], the "snapshots" can equivalently be taken by multiple independent platforms, each with its own physical antenna. The use of multiple spatially distributed antennas significantly reduces the time required for the same operation at the cost of having multiple mobile platforms in operation in place of a single one. Further work [23, 61, 74] has suggested that moving the entire formation over time, similar to the operation of single platform synthetic aperture, can result in even better performance.

Single-Platform Synthetic Apertures

The initial implementations of Synthetic Aperture Antennas consisted of a single antenna system mounted on a moving platform, an illustration of which can be seen in Fig. 2.2.

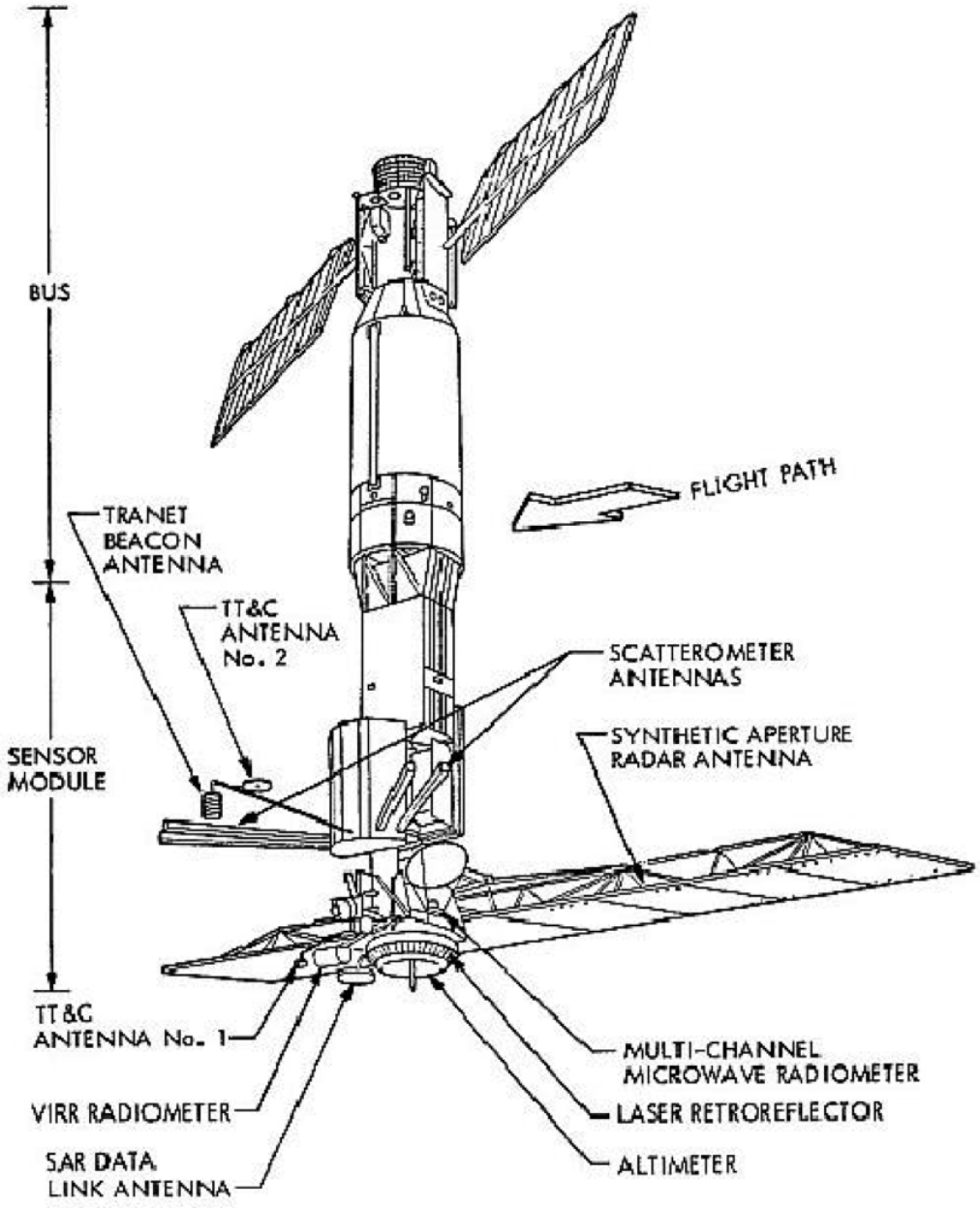

Figure 2.3. *Seasat (Image credit: NASA*[2]*)*

C. A. Wiley helped develop the first SAR [70], which was used for 2D imaging of objects and the Earth's surface using radar. Early work in SAR-based remote sensing was carried out by the military, but after the gradual dissemination of this to the public, civilian implementations were seen, primarily using aircraft.

In 1978, Seasat [39] (shown in Fig. 2.3), the first satellite to use SAR techniques, was launched. Its objective was the detection of ocean waves from orbital altitudes, a mission in which it was unexpectedly successful, as it turned out to also be capable of detecting the wake of submerged submarines. Since then, the use of Synthetic Aperture techniques in satellites has only increased, with numerous current and upcoming programs

[2] `https://www.asf.alaska.edu/seasat/about/`

employing SAR.

Apart from the use of Synthetic Aperture Antennas via aircraft and satellites, current interest in the increased applications of UAVs has also extended to Synthetic Aperture Antennas. For example, UAVs are used for classical SAR using Ultra-Wideband (UWB) [46] or even Millimeter Wave (mmWave) [28], Light Detection and Ranging (LIDAR) [4], indoor radar [72], etc.

For further reference, [4] provides an excellent review of the various application of Synthetic Aperture techniques, which include for example: classic SAR used in Earth observation; Synthetic Aperture Radio Telescopes (SART), a similar technique which utilizes Earth's rotation to move the antenna, and is used for astronomical observations; Synthetic Aperture Sonar (SAS), used in underwater archaeology; and Synthetic Aperture Ultrasound (SAU), used for medical imaging.

Multi-Platform Synthetic Apertures

A relatively newer paradigm in the application of Synthetic Antenna techniques is the deployment of multiple radio-equipped independent platforms in a cluster or swarm. The principle behind this is as follows. In Synthetic Aperture Antennas with a single platform, signals are captured at various positions, and at different times. Processing of the signals is adjusted to accommodate these time variations. This effectively means that the signals can equivalently be received by more than one independent spatially/temporally distributed platforms. Some of the different means to implement this idea are explored in Fig. 2.4.

The feasibility and performance gains from adopting this method are established [8, 18, 23, 61, 74], and include for example, the lowering of hardware performance requirements for each individual radio element, or a reduction in the total time required. In the specific case of SAR imaging, this method provides a larger swath-width, while also allowing for finer resolution, eventually resulting in an overall improvement in the SAR image [61].

Since Earth-observation SAR is often implemented using satellite-mounted antennas, the above discussion readily leads to the concept of a formation of SAR satellites in orbit. The deployment of satellites in a specific formation is relatively easy to maintain given the propensity of the satellites to stay in formation unless disturbed. However, this requires significant resources to set up, both in materials and time.

UAVs on the other hand are significantly cheaper both to manufacture and maintain, and allow great flexibility in operation. UAVs have the downside of having limited range, and less stable formations due to being susceptible to physical effects like wind, along with errors in positioning sensors. Despite this, their flexibility has inspired interest in UAV-swarm-based Synthetic Aperture operations, such as the work in [6, 7, 10, 38]. In order to deal with the most obvious downside of using UAV-swarms for synthetic aperture techniques (i.e. reduced performance due to positional errors in the formation), various

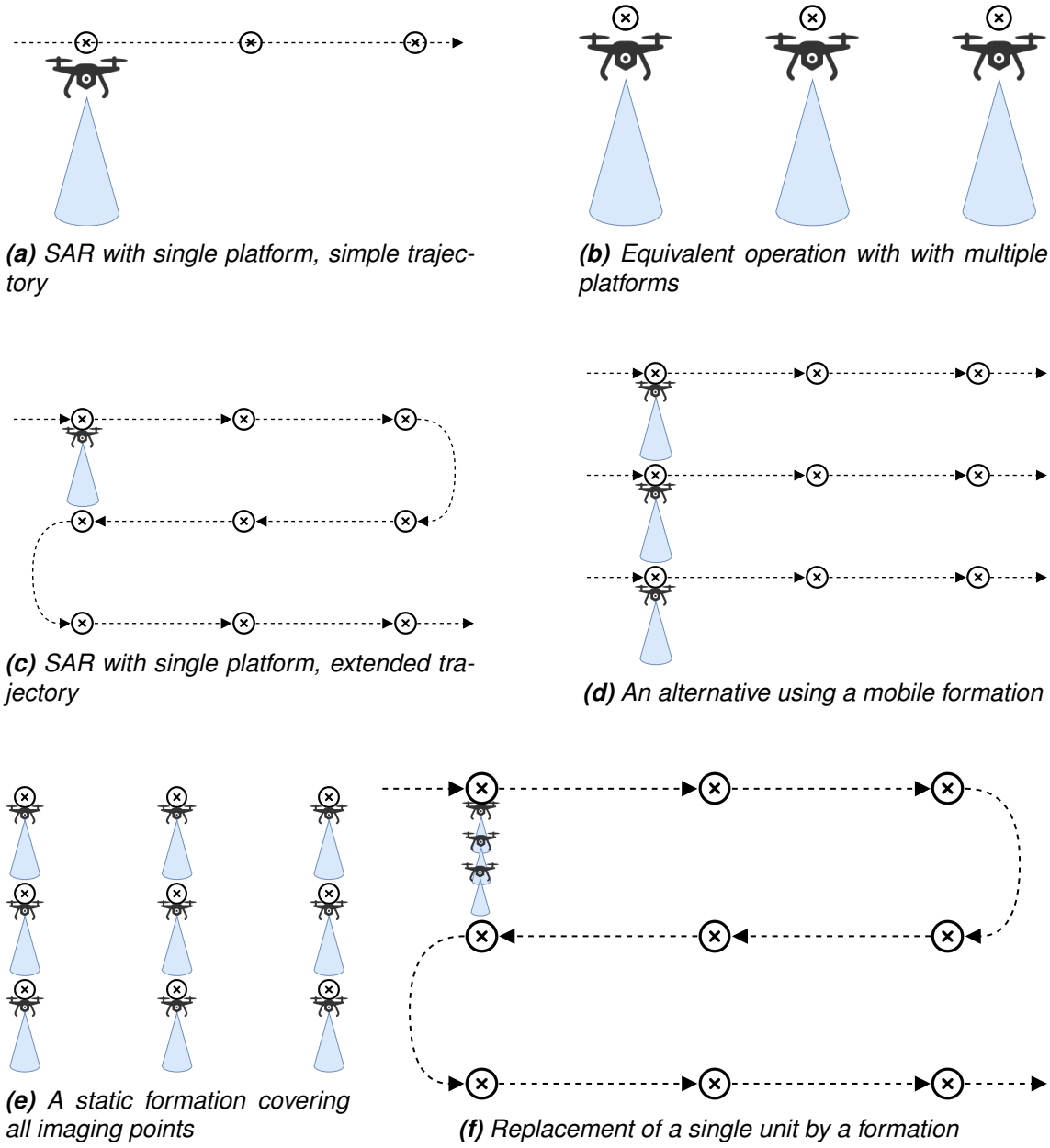

(a) *SAR with single platform, simple trajectory*

(b) *Equivalent operation with with multiple platforms*

(c) *SAR with single platform, extended trajectory*

(d) *An alternative using a mobile formation*

(e) *A static formation covering all imaging points*

(f) *Replacement of a single unit by a formation*

Figure 2.4. *An illustrative comparison of single and multi-platform SAR. Crosses indicate imaging points.*

works [21, 52, 66] have focused on analyzing the position errors and developing ways to compensate for them. This, however, remains a problem that limits the effectiveness of swarm-based antennas.

Effect of Position Errors on Directivity of a Synthetic Aperture Antenna

UAV swarm-based arrays, despite having considerable flexibility, suffer from the drawback of having positioning errors, i.e. deviations from the "ideal" location in the formation. As mentioned previously, these deviations stem from factors such as physical effects like wind gusts and turbulence, as well as errors in positioning sensors.

The effect of these deviations from the ideal position in the formation is to make the antenna less effective. Specifically, the directivity in the intended direction is reduced, while the directivity in other directions is increased instead. Given a fixed link budget, the consequence is to either reduce the range of the Synthetic Aperture Antenna or to require higher transmit power, both being undesirable effects.

Following from the discussion in [7] and [6], the directivity of an end-fire antenna with infinite individual elements is exponentially affected by the variance of the position errors of the elements. Specifically,

$$D = D_0 \left(\frac{1}{1 + \frac{1}{2}\pi \left(e^{(2\pi\sigma)^2} - 1 \right)} \right), \tag{2.1}$$

where D is the antenna directivity with position errors, D_0 is the directivity without errors, and σ is the Root Mean Square (RMS) position error in wavelengths.

Consequently, for increasing RMS position errors, the directivity of an end-fire antenna with infinite elements continues decreasing indefinitely. For an antenna with a finite number of elements, it is noted in [6, 7] that with increasing RMS position errors, the overall directivity matches that of the infinite case closely "until a directivity of a few dB more than the directivity of an individual element is reached".

2.2 Miscellaneous Relevant Concepts

2.2.1 WiFi FTM Ranging

IEEE 802.11mc introduced WiFi Fine Time Measurement (FTM) Round Trip Time (RTT) based range estimation. This was standardized in 802.11-2016 [35] and is also supported by Android Pie [69]. WiFi FTM ranging aims to provide an improvement over traditional Received Signal Strength Information (RSSI)-based ranging, which utilizes the RSSI to estimate the distance from a wireless transmitter.

Compared to FTM ranging, RSSI-based ranging is much more sensitive to environmental attenuation, besides being affected by multipath effects and interference [58]. RSSI-based ranging has also been shown to be affected by coincidental factors like hardware and temperature [5, 47] Further, it is not well suited to real-time ranging due to the time taken to run the scan. FTM ranging however can provide update rates upwards of 3Hz, as noted in [73].

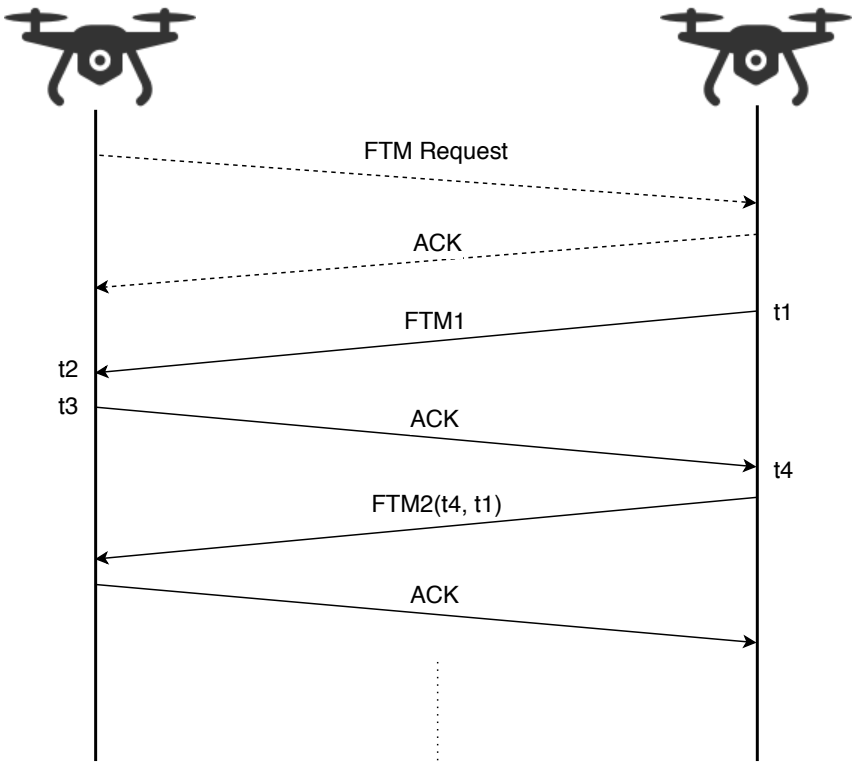

Figure 2.5. *WiFi FTM ranging mechanism*

WiFi FTM Ranging Mechanism

The idea behind WiFi FTM ranging is to use the time of flight of signals between two FTM enabled devices to estimate the distance between them. The FTM process is started when a UAV sends an FTM request message to another, as can be seen in Fig. 2.5. This request receives an acknowledgement message in response.

After a FTM request/response exchange, an FTM message ("ping") is sent by the receiving device, which also registers the time (`t1` in Fig. 2.5). On reception of this message, the requester notes the time (`t2`) and then responds with an acknowledgement ("pong"), whose send time it similarly stores (`t3`). The arrival time of the ACK is also noted (`t4`). The subsequent FTM message additionally contains the timestamps recorded by the receiving device (i.e. `FTM2(t4, t1)`).

Once the requester has all four timestamps, the total RTT can be calculated as follows:

$$RTT = ((t4 - t1) - (t3 - t2)).$$

After the RTT has been determined, the distance between the UAVs can be calculated by:

$$d = \frac{RTT}{2} \cdot c$$

where d is the distance between the transceivers, and c is the speed of light.

The accuracy of this method can be improved by including a number of FTM bursts in a single measurement [34], whose results are then averaged.

It should be noted that a simple one-way trip cannot be used to determine the Time of Flight (ToF), due the presence of differences in clock offsets from "ideal" time. The described process automatically cancels any relative clock error (in terms of offsets), since each of the two messages are affected by the same error in opposite ways.

Accuracy Considerations

Despite the simplicity of the mechanism, in practice the range estimates are subject to errors from sources such as differing clock drift on each drone, RF interference, multi-path effects (e.g. packets transmitted through Non-Line-of-Sight (NLOS) paths tend to report larger distances), calibration errors, etc. The accuracy is further affected by the communication bandwidth provided to the channel, with greater bandwidth improving the accuracy.

In [34], it was determined that meter-level accuracy is indeed achievable provided an open environment with minimal multipath effects. Alternatively a bandwidth of 80MHz can also help to achieve similar accuracy. Another detailed evaluation of WiFi FTM accuracy can be found in [32]. Additionally, further improvements can be achieved by other methods, for example the dead-reckoning techniques as described in [73].

FTM-augmented GPS Positioning

Since the work involves UAV swarms, it is necessary to implement a formation control algorithm. Formation control is, however, a significantly involved topic that grows in complexity with the swarm size. Fortunately, in this work, the focus is on having static formations and keeping them in place. Hence, the formation control can be greatly simplified, since it is not important to have elaborate methods to assemble and move the formation.

Positioning in UAVs traditionally makes use of sensor readings from one or more Global Positioning System (GPS) units, and this is also the case for other works dealing with swarm-based antennas [7, 10]. Using inter-element distance estimation for antenna formation has therefore not been well explored. However, there have been attempts to fuse GPS and WiFi information for positioning, such as [12, 19, 51].

Consequently, in order to provide an advantage over previous works, a simple algorithm has been developed for the purposes of improving formation quality (in terms of positioning accuracy) by making use of FTM-based distance estimates to improve the positions reported by the GPS units. A limitation of this algorithm applies to use cases other than the one in this thesis; the algorithm provides higher accuracy of positioning, but only for specific fixed points (here, the formation destination points). The developed procedure is

now described.

The algorithm is designed to be simple and consists of two main parts, as can be seen in Eqn. 2.2. It calculates an "update vector" that indicates the direction and distance that the UAV should aim to update its position by. In essence, the first term uses differences between the ideal and actual distance between UAVs to decide to move either towards or away from an individual neighbor. The "movements" for each neighbor are summed up, resulting in a value which takes into account all the individual distances. The second term is a simple GPS based vector from the UAV's own actual position to the intended position. Note that the second term does not require any information exchange between individual UAVs, i.e. each UAV assumes its position to the best of its ability. The specific equation is:

$$update = \alpha \cdot (1-f) \cdot \sum_{i \neq j} \left((P_j^{GPS} - P_i^{GPS}) \cdot \left(\frac{d_{ij}^{actual} - d_{ij}^{goal}}{d_{ij}^{goal}} \right) \right) + \beta \cdot f \cdot \left(P_i^{goal} - P_i^{GPS} \right), \tag{2.2}$$

where α and β are numerical constants; $f \in [0, 1]$ is the fraction of reliance of the method on "pure" GPS; P_i^{GPS} is the GPS reported position of UAV i, while P_i^{goal} is the ideal goal position of the UAV in the formation; and finally d_{ij}^{actual} is the "actual" (i.e. FTM-estimated) distance between the UAVs i and j, while d_{ij}^{goal} is the ideal distance between them when in the requested formation.

2.2.2 Drone Modeling

Along with the formation control, another point of relevance is the method employed for modeling the behavior of the UAVs themselves. The simulations in this work make use of the 3DR Iris Quadrotor[3] to model the UAV within Gazebo. This has been chosen since it is the default quadrotor choice for PX4 [4], the flight control software used. The model provides the flight dynamics for use in the simulations, and as such, these can be expected to change in case of a change in the choice of quadrotor model. In terms of sensing, each simulated UAV is outfitted with an Inertial Measurement Unit (IMU) and a GPS unit; no optical instruments are included.

It can be helpful to consider the working of PX4 and the quadrotor model as a black-box. In this view, inputs are fed into the system in the form of mavros[5] messages (for example `https://dev.px4.io/v1.9.0/en/ros/mavros_offboard.html`). In the case of movement instructions, the instruction is encoded as a mavros message, which is then delivered to PX4. PX4 makes use of the selected model (3DR Iris in this case) to calculate the appropriate actuation needed at each rotor, which are therefore the outputs of the

[3] `https://3dr.com/support/articles/iris/`
[4] `https://px4.io/`
[5] `http://wiki.ros.org/mavros`

system. The corresponding thrusts and related physical forces are then simulated by Gazebo, resulting in feedback in the form of updated positions, orientations and forces.

2.3 Methodology

Interest in the operation of UAVs for increasingly varied tasks has been on the rise [29]. As has been discussed in Section 2.1.2, there have been proposals for deploying swarms of UAVs to form highly mobile Synthetic Aperture Antennas. However, this is not a well explored area, and the amount of work considering the actual performance of such antennas in real-world conditions is highly limited.

Consequently, one of the main goals of this work is to evaluate the performance of antennas comprised of static formations of UAVs (as illustrated in Fig. 2.4e). To this end, detailed simulations are to be used which allow for a high degree of realism, in turn producing accurate results.

Having an idea of the end objectives, attention can next be paid to selecting metrics which would help in evaluating and comparing the performance of the different antennas that will be encountered over the course of this study. Once the desired "outputs" of the system are defined, different interesting "input" factors can be selected, which can be expected to affect the performance of the antennas in insightful ways (especially in the context of the selected metrics). Having outlined the "inputs" and "outputs", the design (especially in terms of the flow of data) of the required simulation platform can subsequently be considered.

The upcoming discussion follows the flow of the methodology laid out in the previous paragraph, while also elaborating each part in greater detail. Specifically, the selected metrics for antenna evaluation are considered, followed by the chosen "input" parameters. Next, the simulator pipeline is outlined, connecting the "input" and "output". As a conclusion there is a description of the analysis techniques used for the generated data and a short justification of the various choices made as part of the methodology.

2.3.1 Metrics and Parameters

Selected Metrics

In order to systematically assess swarm-based antennas, their performance first needs to be quantified. This in turn requires the choice of certain metrics which can provide a complete and thorough picture of the antenna performance. In this regard, the following three metrics have been selected:

1. The maximum gain of the antenna, in any direction:

This has been chosen because gain is a fundamental measure of the performance of an antenna; the maximum gain regardless of direction indicates in a sense the maximum effectiveness or potency of the antenna and so higher gain can be considered better.

2. The angular distance between the direction of maximum gain and the intended direction:

   This helps to assess whether the formation has been formed as intended, and whether the antenna is "pointing" in the intended direction. Greater angular distances indicate, in the case of radar, that the imaging will be carried out further away from the ideal direction. In the case of communications, it indicates lower effectiveness of the antenna, and a greater chance of causing interference with other systems. Accordingly, lower angular deviations are more desirable.

3. Relative maximum gain in the main lobe of the radiation pattern compared to side lobes:

   This helps provide a sense of the utilization of energy – having smaller side lobes is important both for efficiency and for reducing interference with other systems. Accordingly, a larger main to side lobe gain ratio is advantageous.

One important point to note is regarding the reason to not include maximum gain *in the intended direction* as an additional metric. The use of the antenna for communications results in the gain in the intended direction becoming one of the primary factors affecting the performance of the antenna, as maximizing the energy received by the receiver is usually the primary aim. However things are different in the case of radar and imaging, where having the maximum gain away from the intended direction only means that the imaging direction is different from the intended one (something measured by the second selected metric); the quality of the results remains unchanged, assuming equal gain.

Since one of the main use-cases of UAV-swarm-based antennas is expected to be radar, the decision was made to not include an additional (communications-centric) fourth metric. Keeping the number of different metrics down also helps avoiding dilution of the attention received by the others metrics. Readers interested in communications are encouraged to replicate the results while including the gain in the intended direction as an additional metric. Further, since the focus is on the quality of antennas formed by swarms of UAVs, factors such as UAV weight, energy consumption, etc. are not considered. Altogether, a combination of the three chosen metrics should allow for a quick assessment of the resulting antenna pattern, which should in turn help in the planning and design of operations that aim to make use of such antennas.

Input Parameters

In order to receive meaningful results, it is essential to select factors which meaningfully affect the performance of swarm-based antennas, and then investigate the precise effects

that variations in these factors have. These factors are to be the main focus of this work, with their effects being analyzed and discussed, also in combination with each other. Due to the large amount of combinations when varying a number of variables, the factors will be split into groups. The effect of each group will be studied in a separate stage, with the best configuration identified from the study of a group being used in the next stage.

At the same time, certain factors are to be identified, which will be held constant throughout the process. These factors are ones which despite affecting the antenna performance, for one reason or another, are not selected to be the focus of the study of this thesis. Specifically, these are:

- FTM ranging configuration parameters
- Drone hardware
- Antenna element design
- Number of drones in the formation (as far as possible)

Each of these has a noteworthy effect on the antenna performance; however, they are not the focus of the work in this thesis. Enough attention has been paid to them to select an appropriate configuration, but the effects of variations of these factors have not been considered. The antenna element design (i.e. the actual antenna carried by each individual UAV), in particular, has been examined to a somewhat greater extent than the other factors on the list. Details of these examinations can be found in Section 4.1.

The factors comprising the first stage of study are now considered. The first of these considerations is that of **formation shape**. Selection of the optimal formation for a given scenario is an extremely involved and challenging task that in its entirety is beyond the scope of this thesis. However, attempts have been made to select a "sufficiently" good formation. Specifically, based on the work presented in [36, 37, 59] supergain arrays are constructed, with the end-fire spacing set to 0.25λ and the front-fire spacing set to 0.85λ. Simple linear end-fire arrays are then compared to possible alternatives, such as having multiple end-fire arrays side by side, such that each layer forms a front-fire array. In the resulting comparison, a special focus is put on their robustness to position errors.

The second factor considered in the first stage is the availability of WiFi **FTM ranging**. Ranging-based distance estimation has so far not been explored in the context of antenna formation, and as such, a special focus has been placed on investigating the performance of different formations with and without the availability of ranging information. Specifically, the different selected formations have been tested under both scenarios in order to ascertain whether certain formations can be made much more effective with the availability of local distance estimation.

After consideration of the above-mentioned factors, a working configuration is arrived upon. This configuration is then held constant, with the second group of factors now being varied. Specifically, these are the operating **wavelength**, and the **wind strength**.

The wavelength has a manifold effect, because it directly affects directly the size of the

antenna (i.e. the formation); changes in the formation size (with the same number of UAVs) correspondingly affect the ratio of inter-element spacing to position error (which remains unaffected), making the antenna more or less sensitive to position errors. A further source of complexity is the effect of changes in formation size on the ability of the UAVs to carry out FTM-based distance estimation. Specifically, increase in sizes might take certain UAVs out of range of others, resulting in reduced availability of inter-element distance estimation, possibly increasing position errors and reducing antenna performance. Finally, the performance with varying wavelength also indicates the suitability of the formation for different tasks (which each have wavelength as an operating requirement).

The second parameter considered at this stage is wind strength. This has been chosen as it is an important real-world effect that affects the ability of a UAV to maintain position accurately. Another rather inconspicuous effect of wind is that even if a UAV manages to maintain position in the face of a gust of wind, a possible tilt involved in holding position changes the orientation of the antenna element on-board, possibly affecting antenna pattern and polarization. Wind as a factor in the operation of swarm-based antennas has been previously considered [7], but in a highly limited manner. The unique capabilities of the developed simulation platform allow for realistic wind effects, paired with realistic reactions on the part of the UAV flight controller, making the consideration of wind as a parameter all the more interesting.

2.3.2 Experiment Process

In the previous sections, the inputs and outputs of the system have been defined, and attention can now be paid to the design of a system which can work within these confines; i.e. generating the desired outputs (the selected metrics) from the inputs (the parameters to vary). An effective simulation platform can fulfill these requirements satisfactorily, and the design of such a simulator is now considered.

This simulation platform is unique in having the ability to simultaneously model physical world effects (like kinematics) and communications (including accurate networking simulations). This presents significant potential in the simulation of UAVs swarms, where inter-node communication is as important as the UAV movement. The unique capabilities of this platform, amongst other things, allow modeling WiFi FTM ranging (which has been used to reduce positioning errors in the formation). Following is a description of the pileline involved in obtaining results.

The first step is to prepare a scenario-specific configuration file, which is read by Gazebo. This includes the initial starting positions for all agents, on the ground. Additionally, coordinates for the destinations for each drone, as per the formation, are provided. This configuration (along with other, more general configuration) is then used to start and run the simulation.

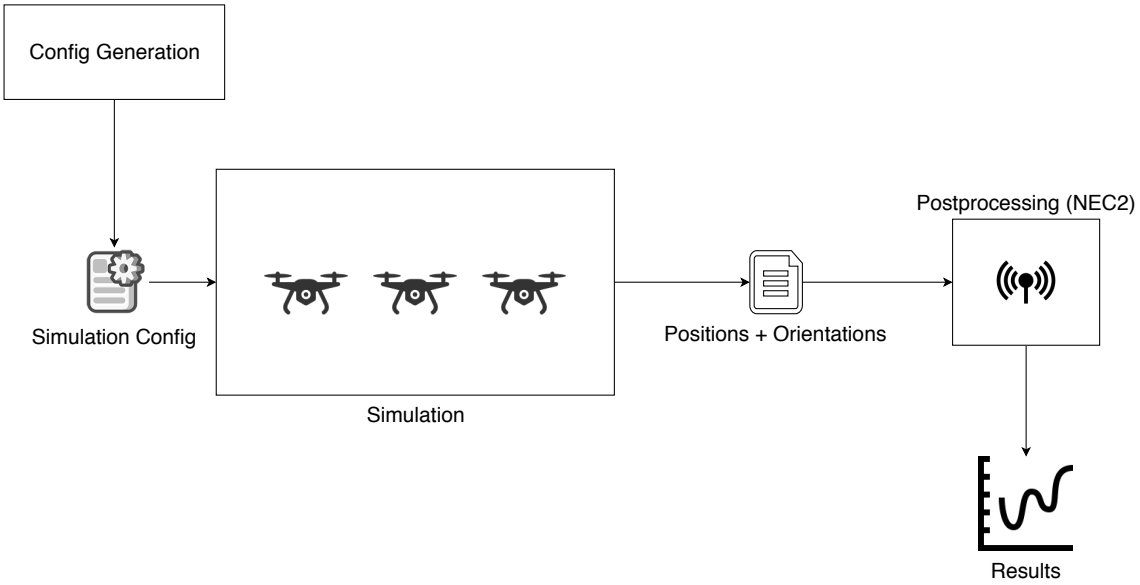

Figure 2.6. *Simulation pipeline*

For the purposes of this thesis, the positions of the UAVs are compared against the destination positions within the formation. Once all the UAVs are determined to be in position (i.e. the RMS position deviations are under a certain threshold), their positions and orientations are sampled for a fixed duration at a set frequency. The idea is to sample the positions and orientations of the UAVs as they attempt to hold position in formation. The UAV position and orientation data from each simulation run is then saved for later processing.

A separate stand-alone postprocessing script has been generated that makes use of the popular NEC2[6] engine for evaluating the antennas formed by the formation (details in Section 3.1.6). For each time instant, the antenna formed by the elements is evaluated according to the previously mentioned metrics. Following this, a Probability Density Function (PDF) plot is generated and saved. This entire process is summarized in Figure 2.6.

2.3.3 Data Analysis Procedure

Once every step in the simulation pipeline has been completed, plots of the selected metrics (i.e. angular deviation, maximum gain, and side-lobe-relative maximum gain) can be generated. Since the selected input factors are varied in two stages, the results are correspondingly generated and studied in two stages. The first stage consists of the effects of formation shape and FTM usage. Here, the maximum gain and the side-lobe-relative maximum gain for each of the selected formations with ideal positions and orientations is first considered, since they provide a baseline for context.

The number of different considered formations is expected to be greater than the different

[6] `https://www.nec2.org/`

values of GPS-weights in the FTM usage, since small changes in this weights are not expected to have significant effects. Therefore, a number of plots are to be generated, one for each value of f, the weight parameter for FTM control. Each of these plots will show the performance for the different selected formations, to facilitate comparison.

These generated plots will then be analyzed in a qualitative manner, in order to provide a better understanding of the mechanisms of the effects of the changes in formations and formation control. Numerical methods are not employed, as the number of simulation runs have been limited due to practical time and hardware constraints. A significantly larger (in time and resources) simulation campaign would be required to provide a high-fidelity data-set suitable for numerical analysis.

Accordingly, the generated plots are examined for apparent trends, for example evident behaviours common to different families of formations, and all observations are compared to each other and to the baseline ideal-case results. A suitable well-performing configuration is then selected out of the variation, which is then employed for the second stage, i.e. the effects of changes in wavelength and wind strength.

In a manner similar to the first stage, plots are generated for each selected wind strength, which depict the performance for the different selected wavelengths. Unlike the first case, neither the wavelength nor the wind strength has an effect on the selected metrics in the ideal case, and subsequently all the results in the second stage have the same baseline results. Accordingly, all variations clearly depict a deviation from the baseline, and are accordingly examined and reported. Inferences are then drawn from the observed trends in the data, and any limitations affecting their applicability are explicitly noted.

2.3.4 Methodology Considerations

One of the choices made as part of finalizing the methodology was the choice to use only static formations, i.e. formations where there is no need for movement of the formation as a whole. The primary reason for this is that moving formations have received considerable attention already, especially in the case of formations of satellites [18, 23]. Additionally, having a static formation allows for equivalent evaluation of their performance as antenna arrays, using a tool like NEC2 – which is highly convenient and reduces the scope for errors. An additional operational advantage provided by this mode of operation is that the total time that the formation needs to be in operation is greatly reduced.

An additional choice here is the decision to make use of a simulation platform. Compared to the use of an analytical model, the use of a simulation allows operation with less assumptions being made, resulting in greater realism. Further, the greater flexibility (e.g. the use of actual flight control software, and allowances for arbitrary formations) and the use of a numerical solver like NEC2 make the results more realistic while also greatly simplifying the procedure, since an analytical solution would usually only allow for specific formations and stochastic error models.

On the other hand, the use of actual hardware and real measurements, of course, provide the most realistic results. However, compared to making use of actual UAVs, the use of simulations allows for much more rapid adaptability (in terms of changing setups), allows for greater control over experiments (e.g. wind speed can be directly controlled in simulations), greater scalability (the number of individual UAVs can be much more easily increased in a simulation), with the added benefit of much lower costs.

The decision to make use of WiFi FTM ranging is based on the fact that WiFi is ubiquitous and has a strong tradition of being used for ranging, e.g. through RSSI. Moreover WiFi-based ranging is also popular, and support for it is even included in Android 9.0 (Pie). This being said, the accuracy provided by WiFi ranging is not the best; actual hardware implementations would benefit from making use of an alternative ranging implementation, such as the UWB-based DW1000[7], which can provide an accuracy of about 10 cm.

An additional choice worth discussing is the use of NEC2 as the antenna modeling system. NEC, originally from the 1970s, is widely used, and is known to generally be a reliable system. It is additionally open-source and freely available on a variety of platforms. Further, in practice it tends to run faster than other, more elaborate tools, making it more convenient to work with. However, there are limitations in the use of NEC2, such as the inability to model dielectric media and their effects on antenna patterns (something which is handled by more modern tools, which however tend to require commercial licenses).

[7] https://www.decawave.com/product/dw1000-radio-ic/

3 EXPERIMENTAL SETUP

This section presents the experimental setup developed for the work in this thesis. Specifically, there is an extensive description of the developed simulation platform, followed by an account of the specific scenarios that were simulated. Note that the simulation platform is the same as the one made use of and described in a previous publication [25], with a few enhancements.

3.1 The Simulation Platform

The operation of UAV swarms involves robotics (including motion control) and high-speed communications besides the actual physical effects that enable flying. Accurate simulations of the behavior of these systems therefore involve correctly modeling each of these aspects along with their interactions. However, currently available simulation software either provides high-fidelity in the physics and sensing aspects – required for robotic interaction; or high fidelity in the communication and networking aspects, but not both [57].

The growing importance and prevalence of mmWave communications has resulted in a number of efforts to model them. Further, modeling mmWave communications especially require accurate dynamics and communications [27, 45, 71]. Numerous efforts have tackled this problem [11, 14, 26, 30, 50, 53, 56], however, these previous works generally deal with specific cases, and each presents a new simulation platform, leaving an obvious gap for a single simulation platform that would encompass all these works.

Additionally, existing models are limited in scope and do not contend with the full complexity of all events that would be required for accurate modeling. For example, channel models such as those described in [40] and [54], are unable to cover all details of multipath channels, such as reflections and Line-of-Sight (LOS) blockage.

Given this background, a simulation platform with the unique capability of concurrent simulation of robotics and network communication systems has been developed with the aim of solving the previously mentioned issues. This simulation platform has previously been used to obtain valuable insights into the Angle of Arrival (AoA) distribution for the case of a radio link between a pair of UAVs engaged in a perimeter surveillance task. The results, along with a description of the simulation platform, have been presented in [25]. A further discussion and description of the simulation platform now follows.

3.1.1 Design Considerations

The Robot Operating System (ROS) framework[1] is currently an ubiquitous choice for the implementation of robotic software. One reason for this is that ROS interacts with physics simulation platforms such as Gazebo, AirSim, or Unity to provide reliable physical and sensor simulations. However, ROS may not provide sufficient support for simulation of the communication between multiple interacting agents. On the other hand, we have communication network simulators such as ns-3, netem, Extendable Mobile Ad-hoc Network Emulator (EMANE), or OMNeT++, which excel at this task.

Accordingly, the focal point of the development of the platform has been to provide an interface between these two distinct simulation tools. This allows for the effective utilization of existing solutions for robotics and network simulations (such as the ones mentioned previously), while providing the high-fidelity simulation required for UAVs. While the proposed architecture is agnostic to the simulator choice, we use a ROS/Gazebo[2] combination for the robotic components and use the WINTERsim mmWave network simulator[3], for the simulation of the communication aspects.

In order to support accurate modeling of mmWave communication, compatibility with current standards that define requirements for such channel modeling has been maintained. Of particular importance is compatibility with the 3GPP Spatial Channel Model (SCM) [1] and 802.11ay channel modeling methodology [48], as they cover the most likely communications options for the mmWave case.

Finally, following from the discussion above, there are two properties of the simulation platform that effort has been put into maintaining. The first is to keep the simulation architecture agnostic to the choice of network simulator. This ensures that almost any network simulator can be used to simulate the working of the actual network, allowing for great flexibility (for example, in practice, WINTERsim and ns3 [9] have been tested to work). The second attribute is (in keeping with the design of ROS+Gazebo), to have the entire simulation architecture transparent to the robotic target application. This allows for seamless deployment to actual physical devices operating with real communications.

3.1.2 Overall Architecture

The considerations listed above lead to a simulation architecture based on two distinct blocks, illustrated in Fig. 3.1. Specifically, there is a robotic simulation component and a network simulation component, which are meant to run concurrently in quasi-synchronous mode (i.e., the relative clock error is constrained). One is tasked with the simulation of network elements (communication), while the other simulates robotic ele-

[1] http://www.ros.org/
[2] http://gazebosim.org/
[3] http://winter-group.net/download/

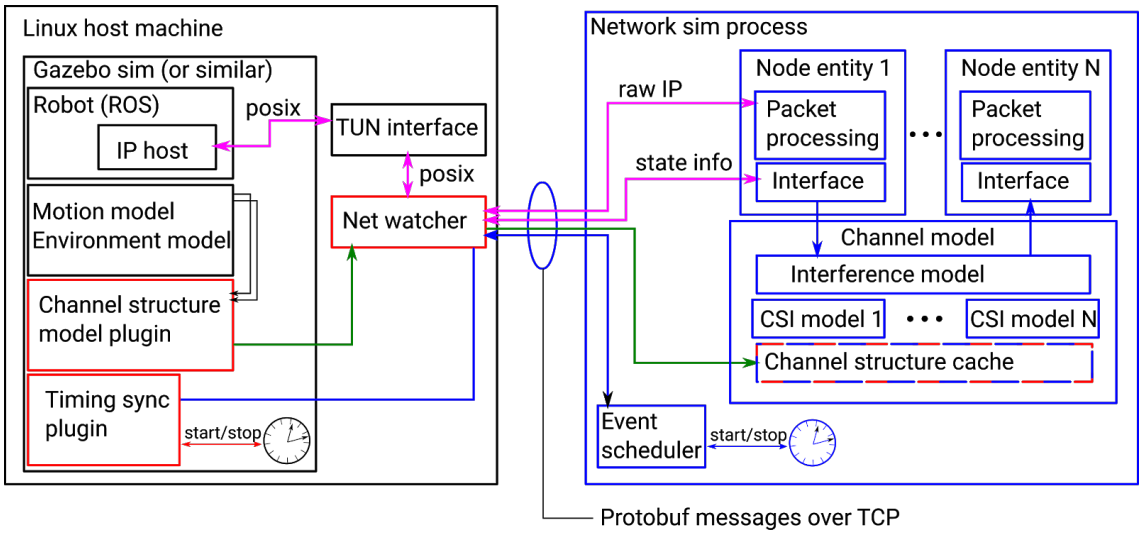

Figure 3.1. *Proposed simulation platform architecture [25]*

ments (physics, sensing, and actuation by way of the autonomous algorithms run by the agent).

These two separate simulation components both require inputs from the other for the mentioned joint simulation. Further, there is a need to maintain time synchronization in each of these simulators to get meaningful results. These functions are implemented by a third component (the NetWatcher). The NetWatcher implements a message passing interface and acts as an orchestrator of the robotic and network simulation components. Effectively, the network and robotic simulators exchange a set of standard messages, allowing for the joint simulation of physics, sensing, actuation and communication, yet without forcing particular software on either end.

3.1.3 ROS + Gazebo Specifics

The robotic simulator is composed of two pieces of software, ROS, and a physics simulator (in this case Gazebo). The ROS is a set of robotic middleware components widely used in the robotic community; the robotic functionalities (e.g. flight control) of the agents are in turn implemented in software that fits into the ROS framework. Along with this, ROS communicates with a physics environment; this physics environment can be modeled by different tools, the most common of which is Gazebo. Gazebo is a 3D simulator that simulates physics, sensing, and actuation. In short, Gazebo simulates the world in which the robotic agents interact. Fig. 3.2 depicts screenshots from some of the simulations used in this work.

The software running in ROS perceives the ROS instance to be a separate host, in the same manner as what it would see with deployment in an actual robotic device. The network interfaces exposed to it are the interfaces of the ROS instance, which are the interfaces of the actual host running Gazebo. To seamlessly integrate the simulated net-

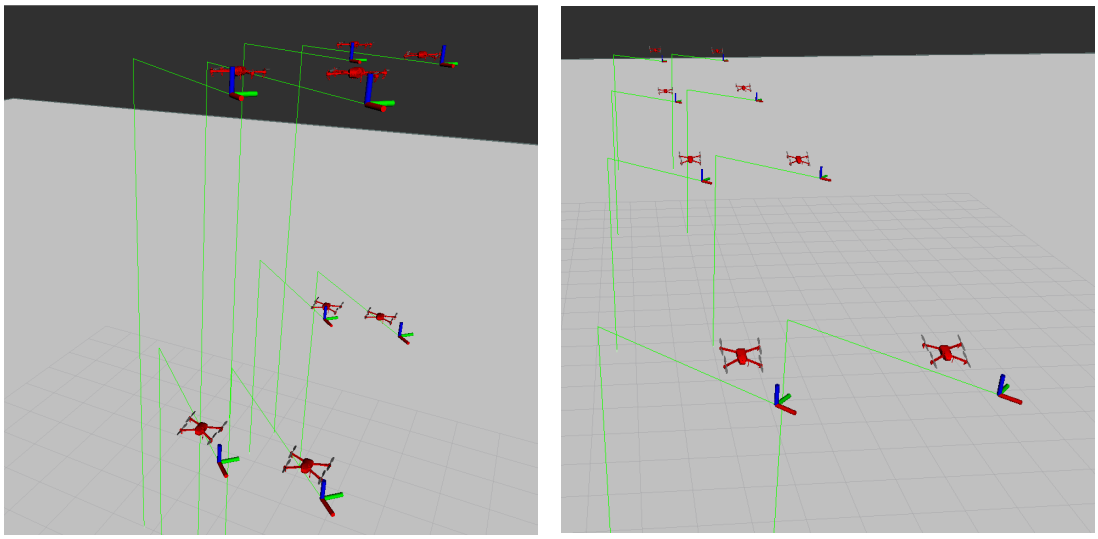

Figure 3.2. *Screenshots depicting UAVs in an ongoing simulation*

work, TUN interfaces (virtual IP interfaces[4]) are used.

The usage of TUN interfaces allows for the ROS components to be unaware that the network, and all communications within it, are in fact simulated (i.e., code during experimental deployment is the same as during simulation). Additionally this fully decouples the network and robotic simulators, allowing any network simulator to be plugged in. In this sense, the robotic agent can perform its functionality without the need to modify its codebase to adapt to the network simulator.

Another point to be noted is that the usage of a robotic simulator in this manner results in a modular structure which allows for a range of channel models to be used; from simple semi-stochastic LOS/NLOS models, to fully deterministic channel models based on “graphics grade” ray tracers found inside physics engines.

Fast Ray Casting

Calculation of the losses from radio effects such as reflection, scattering, diffraction, and transmission (through a medium) requires knowledge of the locations and material properties of all involved objects as well as details of the radio communications used (e.g. carrier frequency).

Gazebo, as the physics simulator, has all this information readily available. To avoid transmitting the complete physical world state (from Gazebo to the network simulator) at every time interval, lookup tables for various interaction losses have been generated. This allows these losses to be calculated on Gazebo’s side while making use of the ray tracer built into Gazebo. Since the calculation of these interaction losses by Gazebo requires a simple table lookup, the time required has been greatly reduced.

[4] `https://github.com/torvalds/linux/blob/master/Documentation/networking/tuntap.txt`

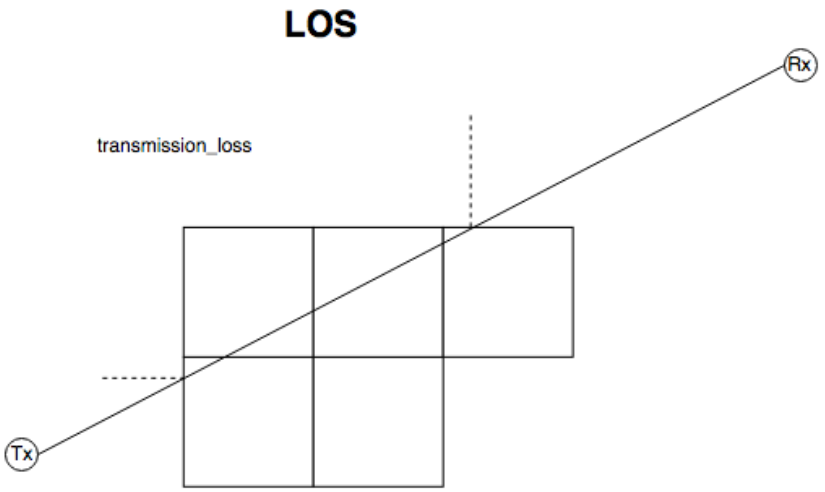

(a)

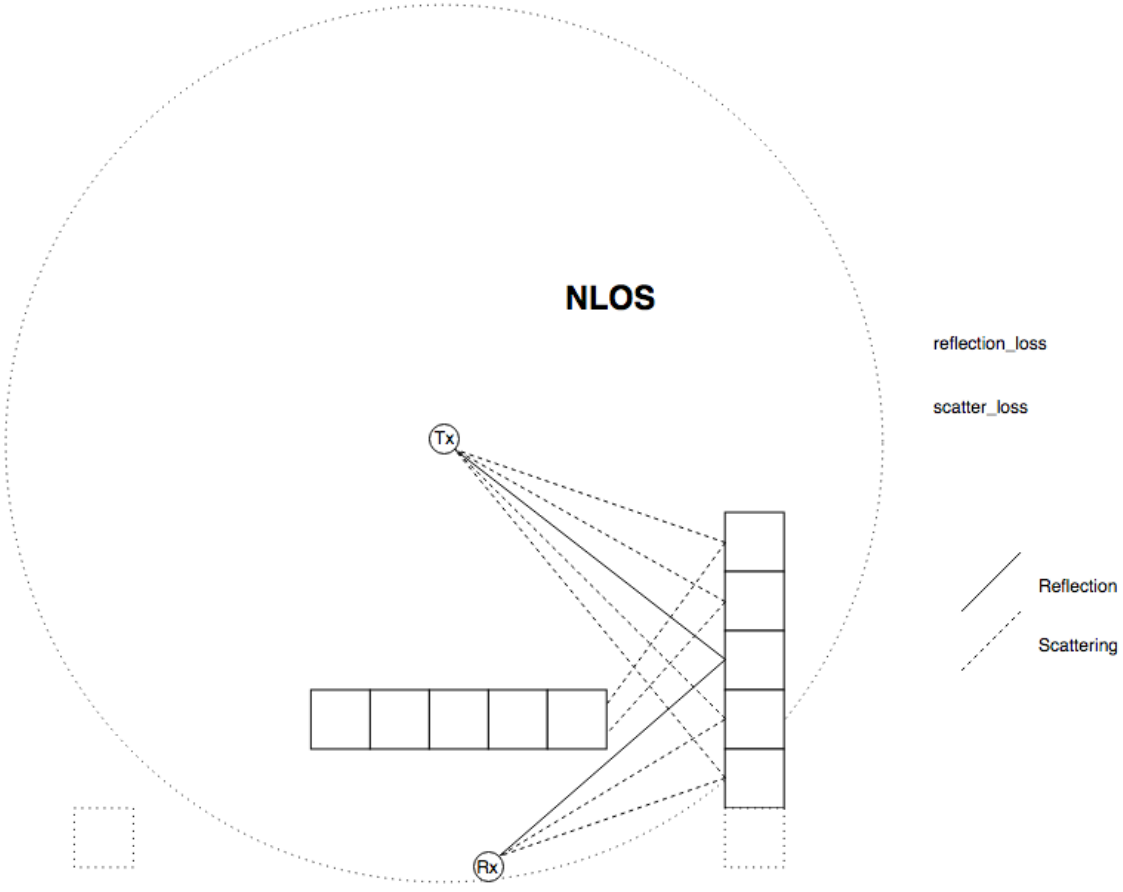

(b)

Figure 3.3. *Interaction loss types (a) LOS: Transmission through a medium (b) NLOS: Reflection/scattering*

The implemented interaction types are, transmission/absorption for obstructed LOS, and reflection and scattering for NLOS cases (diffraction can be implemented as future work). The procedure for the generation of lookup tables is now described. First, a voxel-based physical world is assumed, similar to internal representation of Gazebo. Next, combinations of different material types, carrier frequencies, and incidence and reflection (or scattering) angles are considered. For each of these, the values of losses for reflection/scattering or transmission are calculated and saved.

For every communication, Gazebo uses its internal ray tracer to trace the path of the ray from transmitter to receiver. For LOS/obstructed LOS, a direct path between the two is traced, and any possible transmission losses along that path are calculated. For NLOS, all surfaces within a certain radius are considered, and for appropriate surfaces, the choice between reflection and scattering is made based on incidence/reflection angles.

Depending on the type of interaction (illustrated in Fig. 3.3), if any, Gazebo then looks up the loss for that interaction based on the values in the lookup tables. The calculated losses are transmitted by Gazebo to the network simulator as part of the Channel State Information (CSI). Further details are presented in Section 3.1.5.

3.1.4 Network Simulator Specifics

In the presented simulation architecture, the network simulator is a separate entity, which need not run on the same physical host as Gazebo+ROS. All communication from the network simulator is directed to the NetWatcher, which in turn communicates with Gazebo+ROS. This provides the network simulator with a single point of contact which abstracts away all implementation details of the robotic simulator.

The principle of operation of the network simulator is as follows. The network simulator runs an internal simulation as usual. The modifications needed for concurrent and integrated simulation with Gazebo occur at a few well-defined points. First, the timing control mechanism is set to be closely directed by the implemented time synchronization mechanism (described in Section 3.1.5), advancing only when indicated. Secondly, the internal channel models are supplemented with detailed CSI from Gazebo (details in 3.1.5). Lastly, packets generated by individual robotic entities are to be routed through the simulated network, and for this, IP packets are created in the network simulator accordingly.

The IP packets sent from one robotic entity to another are intercepted at the network layer through the use of virtual IP interfaces (i.e. TUN interfaces). The use of a layer 3 interface is a deliberate choice in order to reduce unnecessary complexity. Specifically, this enables supporting arbitrary IP communications between arbitrary applications through the simulated network, while abstracting away all details below the network layer.

Simulator Flexibility

Due to the modular and decoupled nature of the platform architecture, any network simulator capable of communicating with the integration infrastructure (the NetWatcher) using predefined protocols can be plugged in. This can range from a simple single-file script to full-fledged network simulators such as WINTERsim and ns3.

The event-driven WINTERsim network simulator, has been used for network simulations for the purposes of this thesis, and also in [25]. It was primarily chosen due to its unique support for high-fidelity channel modeling. The advanced multipath model implemented in this simulator has been presented in [55]. By replacing the stochastic channel state with actual data from Gazebo+ROS, the capability of a fully-featured network simulation platform was leveraged.

ns3 is one of the most widely used open source network simulators, and significant effort has been spent on its development. In order to demonstrate the flexibility, and increase the accessibility of the simulation platform, support was added for ns3 as the network simulator. This primarily consisted of adding support to ns3 for the custom protocols for time synchronization and packet handling. Due to current limitations in ns3's support for detailed channel models, the CSI provided by Gazebo+ROS was not incorporated. However, the full range of ns3's available stochastic channel models can be used instead.

3.1.5 NetWatcher Specifics

The NetWatcher, as mentioned previously, is the central component that coordinates the operation of the two simulators, passing both data and control messages from one to the other and ensuring that the clocks on either end remain in sync.

The NetWatcher acts as a single point of contact for all purposes for both the simulators, which never directly communicate with each other. This greatly simplifies the implementation of all necessary communication besides providing a clean point for alternate simulators to be plugged in, as previously discussed.

The NetWatcher is implemented as a multithreaded application, and since the NetWatcher needs to be able to modify the interfaces available to Gazebo, it is constrained to run on the same physical host as Gazebo. Following is a description of the various functionalities implemented by the NetWatcher component.

Time Synchronization

Since it is possible to run the presented simulation platform in a distributed manner, it is of the utmost importance for there to be some sort of mechanism to ensure that the passage of time in the simulations in both simulators is synchronized. Differences in the rates of

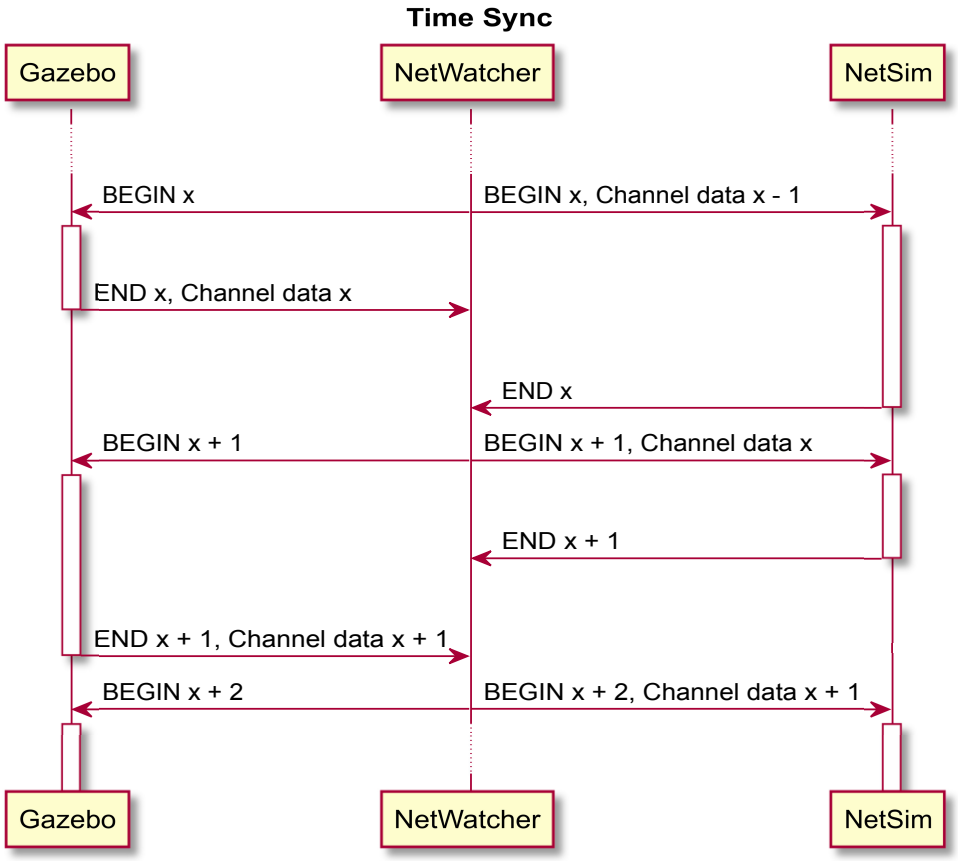

Figure 3.4. *Time synchronization mechanism*

the passage of time in the two simulations stem from multiple factors. First and the most obvious is that both the simulators process different events, and being event-driven, might have a differing number of events in a given time interval – leading to differing real-world run times per interval, even assuming equal event processing times. A second possible cause is the difference in the time taken by the actual processing needed for any given time interval. Thirdly, differences in the offsets of the internal clocks on the physical host running each simulator, and possible time drifts can also result in different simulation times on each simulator.

The mentioned factors show the importance of having some synchronization/time-sharing mechanism. Failing this, it might happen that at any instant (in "real" time), each simulator is at a different point in simulated world time. Since each end simulates a different aspect of the world (i.e. physics and communications), this can result in completely invalid results. For example, time passing faster or slower for communications than for UAV movement, or messages being delivered to the past.

Time synchronicity is maintained by having the NetWatcher control and co-ordinate the flow of time in both Gazebo and the network simulator. Specifically, the NetWatcher, as the central component, declares the start of a time interval and informs both simulators of the same. Each simulator then proceeds to the indicated interval, whose length is fixed (and configurable). As and when each simulator is done, it notifies the NetWatcher. The

NetWatcher waits for acknowledgements from both ends before proceeding to the next interval. This mechanism ensures that relative clock error in both simulators is constrained to the length of the time interval.

The specifics of the protocol used are now described. `BEGIN` and `END` messages are defined as messages in Google's Protobuf[5], which facilitate the synchronization through the described protocol (also illustrated in Fig. 3.4). Simply, a `BEGIN[x]` message indicates that the recipient can begin time interval `x`; `END[x]` indicates that the sender has completed processing for interval `x`, and is ready for interval `x+1` to begin.

To mark the beginning of a time interval, the NetWatcher sends a `BEGIN` message to both Gazebo and the network simulator at the same time. Gazebo and the network simulator reply with an `END` message when they are ready to proceed. The NetWatcher then waits for both `END` messages before sending the next `BEGIN` message. This ensures that Gazebo and the network simulator run in sync.

The length (in simulated time) of each interval is configurable. Smaller intervals mean more close synchronization, i.e. higher accuracy. However they also introduce more overhead, since a greater fraction of time is spent dealing with the control mechanism. Conversely, larger intervals have better efficiency and allow the simulation to run faster, but also allow for greater possible relative clock error, making results less accurate. An interval size of $10ms$ was found to be a reasonable middle ground in terms of performance and accuracy; consequently, this is the interval used for all results here and in [25].

TUN Operation

An important part of the functionality of this simulation platform is that arbitrary communications (in practice, IP packets) between individual simulated UAVs need to have corresponding packets travel through the simulated network in the network simulator. Since ROS implements a full network stack and allows running actual flight control software, the IP packets that would need to be transferred are fully formed and legitimate. These packets need to be intercepted, and the network simulator has to be signalled to create an equivalent network packet. The mechanism for accomplishing this is now described.

Since Gazebo exposes the actual interfaces on its physical host to each of the ROS instances, the interfaces used by the UAVs need to be actual interfaces on the host (Specifically, the software on a UAV will bind to an IP address, and use that for all communications. This IP in turn needs to be available on the physical host running Gazebo). To this end, the NetWatcher sets up a number of virtual network interfaces (TUNs) which are seen and used by the individual robotic applications as actual interfaces to the simulated network, i.e., they send and receive packets in a standard manner. In order to accomplish this, the NetWatcher spawns a number of threads, each of which watches one TUN interface for incoming packets.

[5] `https://developers.google.com/protocol-buffers/`

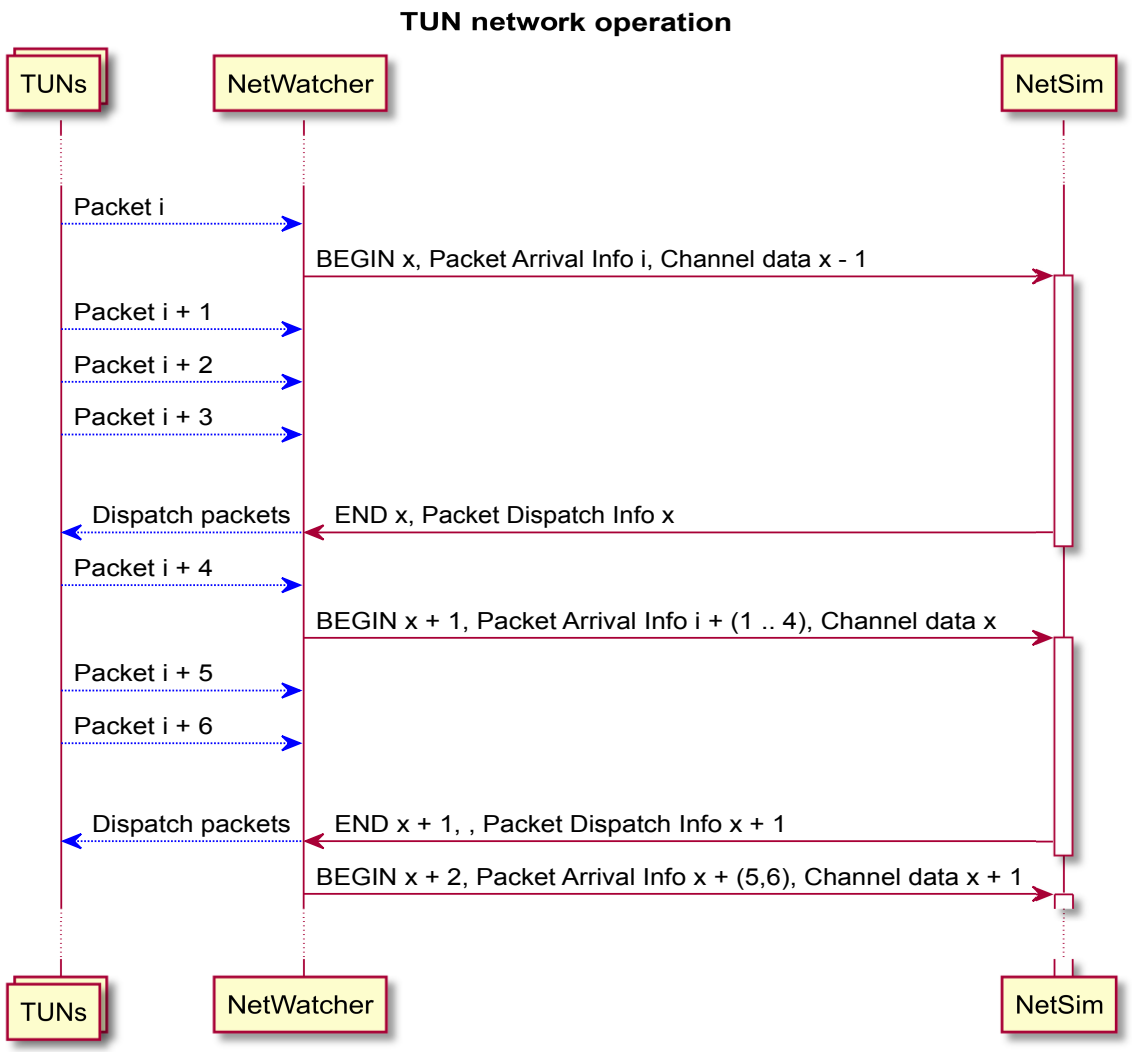

Figure 3.5. *TUN network operation*

As an interesting side note, it can be observed that by default all Linux hosts apply an optimization for the quick delivery of packets travelling between two interfaces on the same host. This optimization is the use of the local loopback interface for the routing of such packets, regardless of the actual requested interface. Use of the loopback means that the packet skips much of the network stack resulting in much faster delivery. However, this optimization needs to be circumvented to allow packets from one simulated UAV to another to actually travel through the simulated network. For this purpose a mechanism to conditionally apply local loopback routing based on the incoming interface was added to the NetWatcher.

Now continuing on with the description of the TUN operation, on receiving a packet, the packet is buffered by the NetWatcher and its signature (a unique numeric id, source IP address, destination IP address, packet length) is scheduled to be transmitted to the network simulator (note that the packet itself is not transmitted). At the beginning of the next time interval, all accumulated packet signatures are sent to the network simulator along with the `BEGIN` message for that time interval. The network simulator then creates

an equivalent packet in its own internal simulated network based on the packet signatures delivered to it.

On delivery of the packet to any host in the network, a notification of delivery is then scheduled to be transmitted back to the NetWatcher. Note that a single packet can be delivered to multiple hosts. For this reason, the NetWatcher keeps the packet buffered even after delivery. Once a packet has completed its movement through the network (e.g. resulting in being delivered, dropped, or lost) with no further events, a notification for deletion (from the internal buffer) is scheduled (to prevent memory issues, automatic deletion with a reasonable timeout is also scheduled).

At the end of processing of any given time interval, the network simulator generates an `END` message as usual, and additionally includes two lists, one for delivery notifications, and one for packets ready for deletion from the buffer. The delivery notifications consist of the packet signature, the recipient, and the Bit Error Rate (BER) to be applied to the packet. Notifications of packet deletion consist only of the packet signature.

Upon receiving an `END` message with accompanying packet data, the NetWatcher applies the indicated BER, and forwards (or drops, based on the BER) the packet to the right TUN, at which point the packet is received by the listening robotic application. Packets are also removed from the internal buffer based on received deletion requests or on timeout. An illustration of the entire process can be seen in Fig. 3.5.

This mechanism allows the network simulator to directly control the packet delay and BER seen by the robotic applications. Additionally, it should be noted that since the packet arrival/dispatch information is only sent with `BEGIN/END` messages, the granularity of packet delay that can be introduced is limited to the chosen time interval length. This has been designed to improve CPU utilization for the network simulator, while maintaining sufficient control over the introduced delay.

Apart from actual packets, the NetWatcher also assigns parameters to the virtual network interface internal state (IP address, subnet, up/down state, etc). In this way, complete network emulation (running in the same simulated time as the ROS) is presented to the target robotic applications.

CSI Format & Transfer

One of the unique features of the developed platform is the use of highly detailed and realistic CSI in the network simulator in order to provide accurate communications in the simulation. In order to do this, the detailed physical world information available in Gazebo is used for accurate ray-tracing, as discussed shortly in Section 3.1.3. This mechanism allows for the generation of CSI that allows for detailed multipath and multihop radio propagation between individual UAVs in the simulation. While Section 3.1.3 discussed the use of lookup tables to generate losses in Gazebo, further details of the generation of the CSI are now considered.

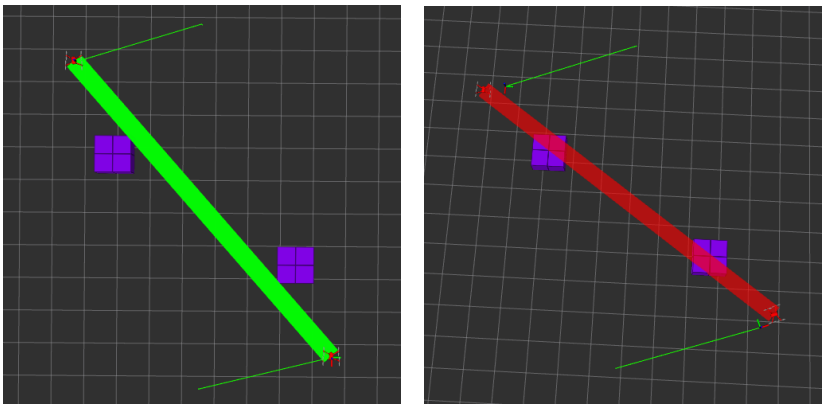

Figure 3.6. *A sample channel representation in ROS consisting of a LOS (left) and NLOS (right) check on a 3D occupancy grid with two pillars.*

The detailed 3D simulated environment in Gazebo is first transformed to an OctoMap [33], which is a 3D occupancy grid similar in nature to a voxel-based system. Raytracing is then performed in this 3D occupancy grid (a simple example is shown in Fig. 3.6), which generates detailed multipath and multihop 3D CSI. Specifically, node positions, orientations, and all propagation paths (consisting of the availability of LOS, and all hop points and interaction losses) are generated.

It should again be emphasized that this eventual abstraction into a 3D CSI format allows for the use of a range of channel models starting from simple LOS/NLOS, to highly accurate multi-hop raytracing. Additional points to note are that the complete trajectory and intermediate interaction losses of all multihop paths are generated in a deterministic manner, requiring no use of stochastic models in the network simulator. It should also be pointed out that only material interaction losses are calculated and transferred as part of the CSI. Path loss is still calculated for both LOS and multihop paths based on the trajectories in the CSI.

Gazebo generates the CSI as described, following which it is encoded using a predefined Protobuf message. This message is in turn encapsulated as raw bytes within the time synchronization Protobuf message. At the end of every time interval, Gazebo sends the generated CSI to the NetWatcher, along with the interval's `END` message (see Fig. 3.4). The NetWatcher then forwards this data to the network simulator with the succeeding `BEGIN` message, where the encapsulated CSI Protobuf message is extracted and decoded. This mechanism allows the transfer of CSI from Gazebo to the network simulator without the need of any extra messages, which simplifies communication.

Driver-Level Operations

In order to further extend the capabilities of the simulation platform, and to provide greater realism and control, a mechanism has been implemented to allow dealing with "driver"-level functionalities such as WiFi FTM ranging, and WiFi scanning. Note that for the

purposes of this thesis, actual implementation has been restricted to WiFi FTM ranging, but the architecture provides for simple extensibility to include other features.

The implementation has been made along the lines of netlink sockets [16], which are used to transfer messages between kernel modules and user-space processes in Linux systems. A similar socket-based setup is used in the simulation platform, with the messages using JavaScript Object Notation (JSON) in place of the netlink protocol. JSON was chosen here mainly for its flexibility and simplicity. For each simulated network interface, a socket is exposed by NetWatcher to which the flight control software can send requests (e.g. for FTM ranging to an interface on another UAVs), and from where it also reads responses.

Internally, the NetWatcher aggregates the requests it reads on these sockets, and at a set frequency, transfers all received requests to the network simulator on the other end, which deals with these requests (e.g. by initiating FTM ranging between the simulated interfaces) as per its internal logic. At a set frequency, the network simulator checks for any responses ready to be written back to the pseudo-netlink sockets, and transfers the same to the NetWatcher, which in turn writes the response to the appropriate socket. Currently, implementation to deal with these "driver-level" requests has only been completed in WINTERsim.

3.1.6 Postprocessing

For the purpose of the work in this thesis, a stand-alone postprocessing script was constructed, which serves to provide an analysis of the performance of a simulated antenna. Specifically, within the simulator, once the drones are determined to be in position (via position errors being under a threshold), 10 seconds of position + orientation data is recorded. This data is then saved, and read by the postprocessing script.

The postprocessing script, for each time instant, reads the positions and orientations of all drones. This data is used to generate the exact geometric coordinates for the antennas carried by the drones. The next step is to determine the phases of the excitation voltage applied to each antenna. For this, a simple and flexible method is employed, which is as follows: A single direction is chosen to be the intended direction of maximum gain. The phases of individual elements are then set so as to add up constructively at a distance of 100 times the wavelength in the chosen direction, assuming the antenna elements are present at their ideal positions. While this phase selection method attempts to ensure constructive interference in the intended direction, it does not attempt to factor in other requirements, such as the minimization of side-lobes.

Once the antenna positions and excitation details are ready, these values are fed as input (via a python Application Programming Interface (API)[6]) into NEC2 (a well-known, reliable, and widely-used antenna modeling tool). The far-field gains of the system are

[6] https://github.com/tmolteno/python-necpp/tree/master/PyNEC

then computed as a function of the azimuthal and polar angles. From the gain information, the values of the three selected metrics (described in Section 2.3.1) are obtained. This process is repeated for each recorded time instant, at the end of which, the PDF (i.e. likelihood distribution) of each of the metrics is calculated and plotted.

Main Lobe Detection

One of the selected metrics is the difference between the maximum gains in the main lobe and the side lobe. Therefore, there is a need to have an automated and consistent way to identify the main lobe of an antenna given its radiation pattern and intended direction of transmission. This has been achieved by making use of automated contour generation, followed by filtering of the generated contours.

The process is as follows: the radiation pattern of an antenna is obtained as a 2D matrix, with the two dimensions corresponding to the horizontal and vertical angles. This is then

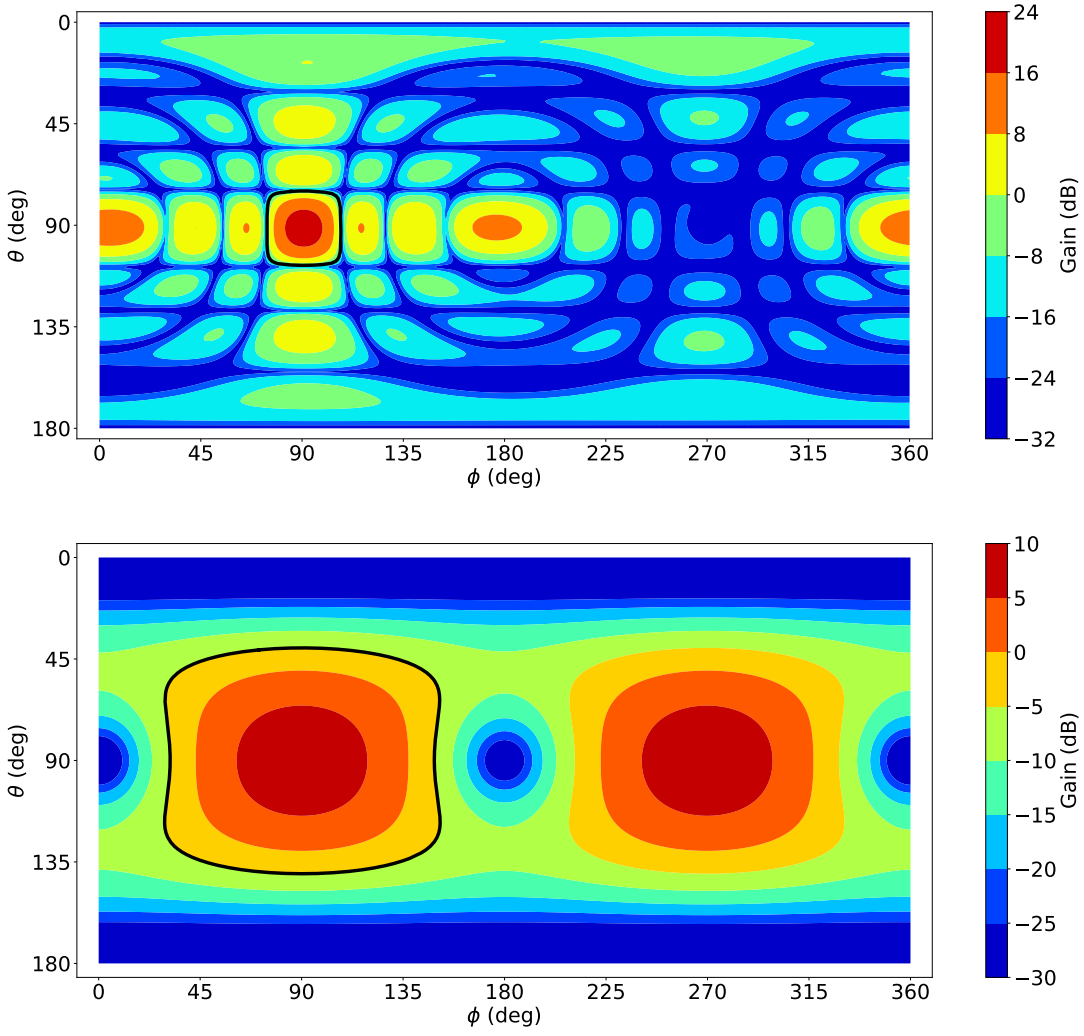

Figure 3.7. *Examples of main lobe detection*

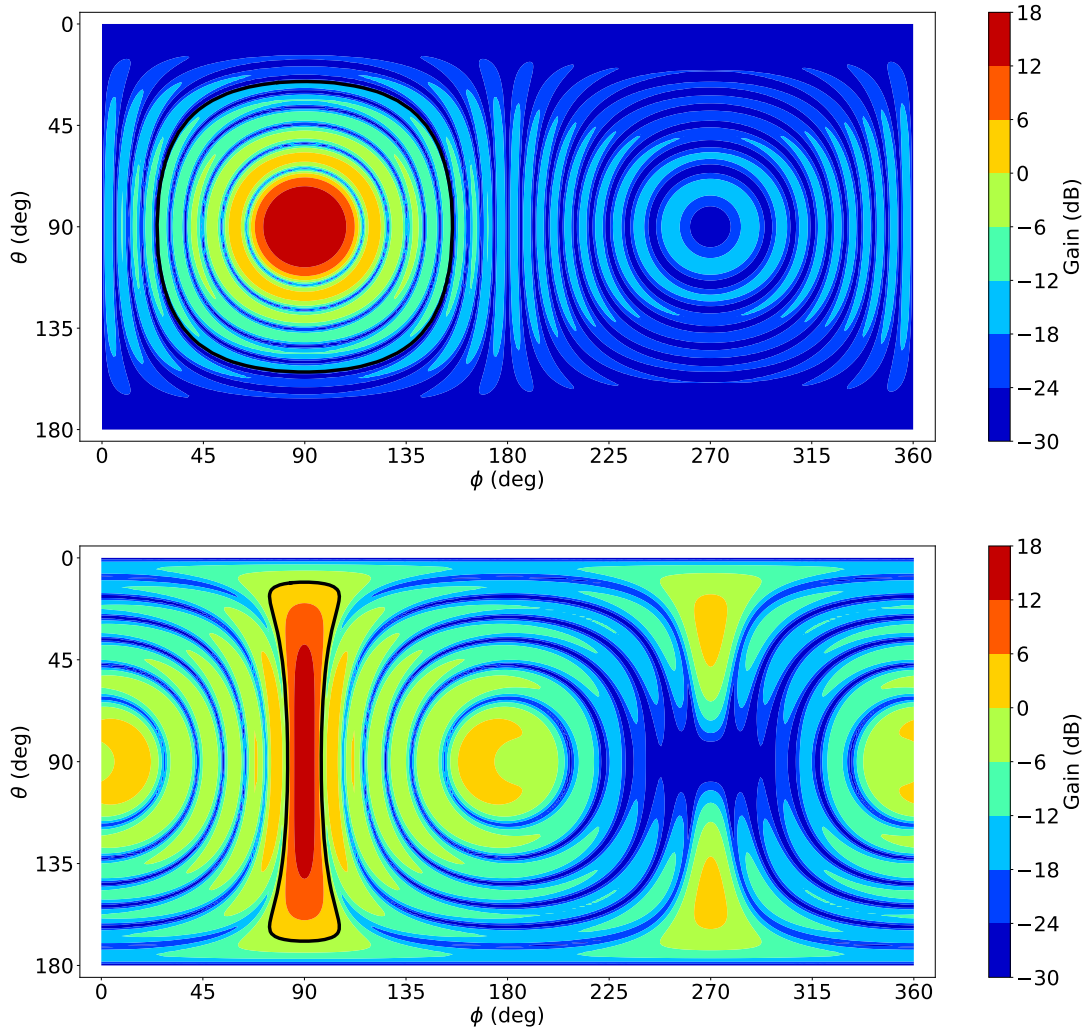

Figure 3.7. *Examples of main lobe detection (cont.)*

fed to a contour generation function. The generated contours are then filtered based on the following criteria: being a valid closed polygon; containing the direction of intended transmission; and being close to convex (some leeway is provided). The resulting set is then searched for the largest containing polygon, which is then identified as the boundary of the main lobe. Some examples of the working of this procedure are shown in Fig. 3.7; the detected main lobe is outlined in black.

3.2 Simulation Details

In each simulation scenario, the simulated world consists of an open area with no obstacles. The UAVs start off on the ground, with their initial position based on the final goal positions in a manner so as to avoid path overlapping. All agents take off simultaneously and make their way to the goal positions. Once the UAVs are more-or-less in position (a configurable distance away from goal), command passes to the formation control algo-

rithm which attempts to maintain formation and reduce position errors, possibly making use of FTM ranging data.

Each simulation run is configured with a number of parameters, four of which are varied for detailed study. Specifically, these are: the formation; f – the FTM control parameter; the operating wavelength; and the wind strength. As indicated in Section 2.3.1, the variations are split into two stages. The first stage varies the formation and the FTM control parameter together; they make use of a mild wind strength of $2N$ and a wavelength of $10m$. The second stage varies the wavelength and the wind strength. Now follows a description of the variation of these parameters along with the underlying motivations.

First is the selection of the formation that the UAVs are to be arranged in. The selection of the formation is the most involved of the four input factors, as the others simply consist of a variation of a numerical parameter. Supergain effects, as described previously, are leveraged in the construction of the formations. The target is therefore to have end-fire arrays with an inter-element spacing of $\frac{\lambda}{4}$, and front-fire arrays with a spacing of 0.85λ, where λ represents the wavelength.

Due to temporary technical constraints, the maximum number of UAVs available for simulation has been limited to 10. In order to mitigate the effect of a differing number of antenna elements, it would be ideal for all considered formations to contain the same number of elements; however, this might exclude some interesting formations – for this reason a difference of up to 1 element will be considered. It is also important to not over-inflate the number of formations to avoid a dilution of attention. Given these constraints, the specific formations considered are:

- 8 element linear end-fire
- 2 end-fire arrays of 4 elements each
- 3 end-fire arrays of 3 elements each, in a triangular formation
- 4 end-fire arrays of 2 elements each, in a square formation
- 3 end-fire arrays of 3 elements each, in a flat formation
- 4 end-fire arrays of 2 elements each, in a flat formation

These formations are visualized in Fig. 3.8, with the blue spheres representing the antenna element positions, and the red arrow representing the direction of transmission.

One interesting alternative for the flat formations is to have them arranged in a vertical plane instead of a horizontal one. This has no difference with an isotropic antenna element, but it does in the case of an omnidirectional one. Specifically, the effect is to have smaller side lobes, but also lower maximum gain. There is also a slight increase in operational complexity compared to a horizontal formation, where each UAV has the same altitude. For these reasons the horizontal flat formations are considered instead.

The custom formation control algorithm that has been employed in this work has been described in Section 2.2.1. The parameter f, as mentioned represents the weight given

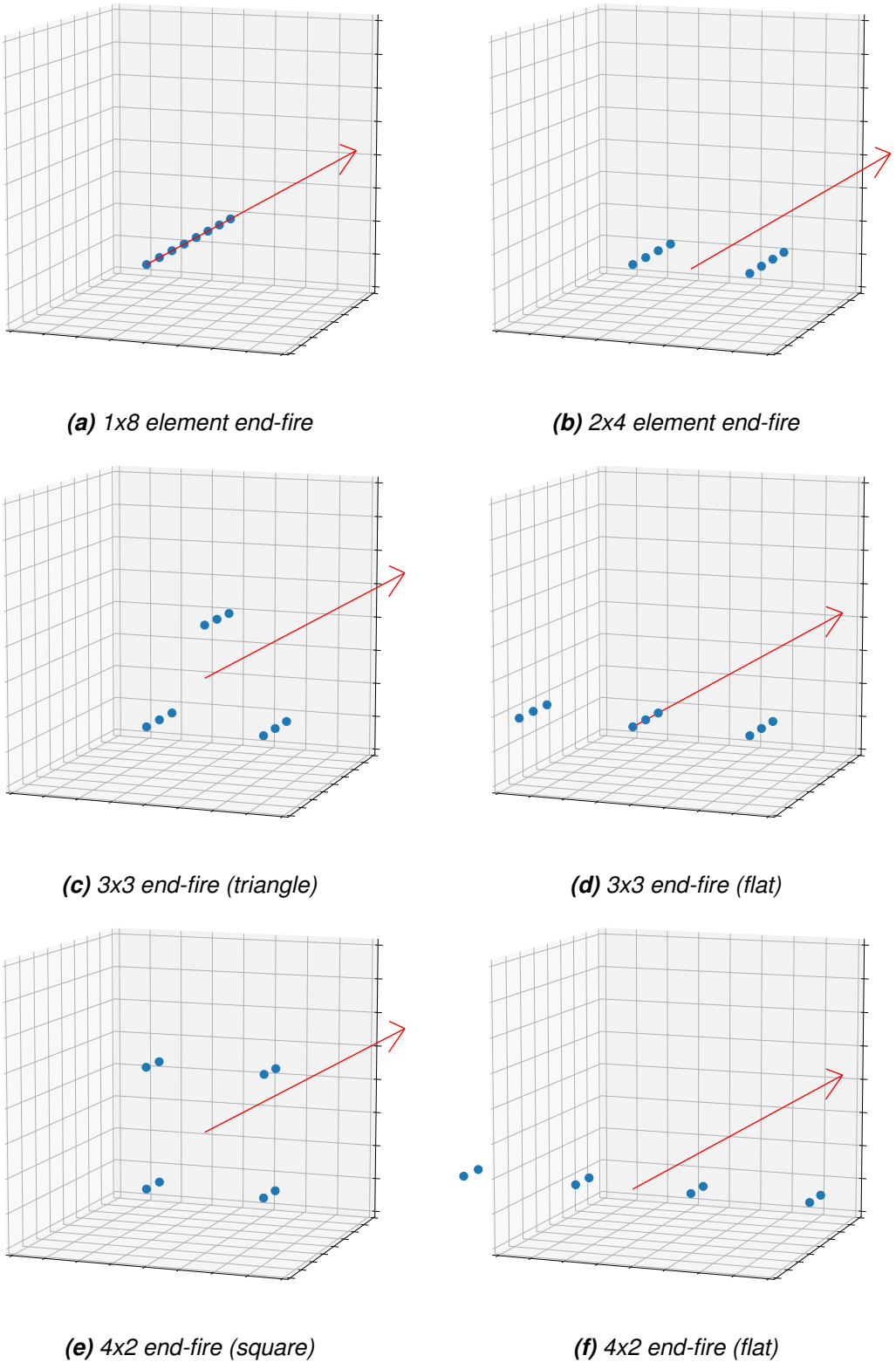

(a) *1x8 element end-fire*

(b) *2x4 element end-fire*

(c) *3x3 end-fire (triangle)*

(d) *3x3 end-fire (flat)*

(e) *4x2 end-fire (square)*

(f) *4x2 end-fire (flat)*

Figure 3.8. *The different considered formations*

to straightforward GPS positioning. An f value of 1 implies pure GPS, while 0 employs exclusively FTM. f is therefore one of the input factors whose effect is to be studied. Since small changes in this value are not expected to yield significant results, and since evaluating a large number of values is impractical (since each formation must be examined for each of these values), three separate points are chosen. The details of the selection of these points are reported in Section 4.1.

The first parameter of the second stage is the operating wavelength. The wavelengths tested are $5m$, $10m$, $15m$, and $20m$, which correspond to the wavelengths of 60, 30, 20, and 15MHz. Shorter wavelengths make it impractical to achieve supergain effects, while longer wavelengths have reduced applications that might require mobile antennas. The selected wavelengths fall into the range used by e.g. GPR and OTH-Radar. Additionally, they provide an appropriate demonstration of the validity of the methodology.

The last parameter is the wind strength. The wind is modeled in Gazebo, which is able to make use of a variety of different wind models via different available plugins. The specific wind model used in this work is the default wind plugin[7] for PX4. In this model each agent has its own wind distribution, and at each physics update, a sample from the distribution is generated and the resulting wind forces are applied to the agent. In this sense, this model is similar to the one used in [7] and is as such in line with similar work. The specific values for mean wind strength that have been used are: $0N$, $2N$, and $5N$. These are chosen to provide a representative distribution from almost still air to a brisk wind. Larger values generally cause serious trouble in movement.

The degree of realism of the wind in the simulation can be improved by replacing the mentioned wind model with a more elaborate and versatile wind plugin, such as the one provided in the RotorS library[8]. Due to resource constraints, this is left as an enhancement for future work.

[7] `https://github.com/PX4/sitl_gazebo/blob/master/src/gazebo_wind_plugin.cpp`
[8] `https://github.com/ethz-asl/rotors_simulator/wiki/Adding-a-custom-wind-field-to-your-world`

4 RESULTS AND ANALYSIS

4.1 Parameter Selection

This section describes the selection of appropriate values for parameters which are to then be held constant for the rest of the work, as per the outline laid out in Section 2.3.1.

Formation control parameters

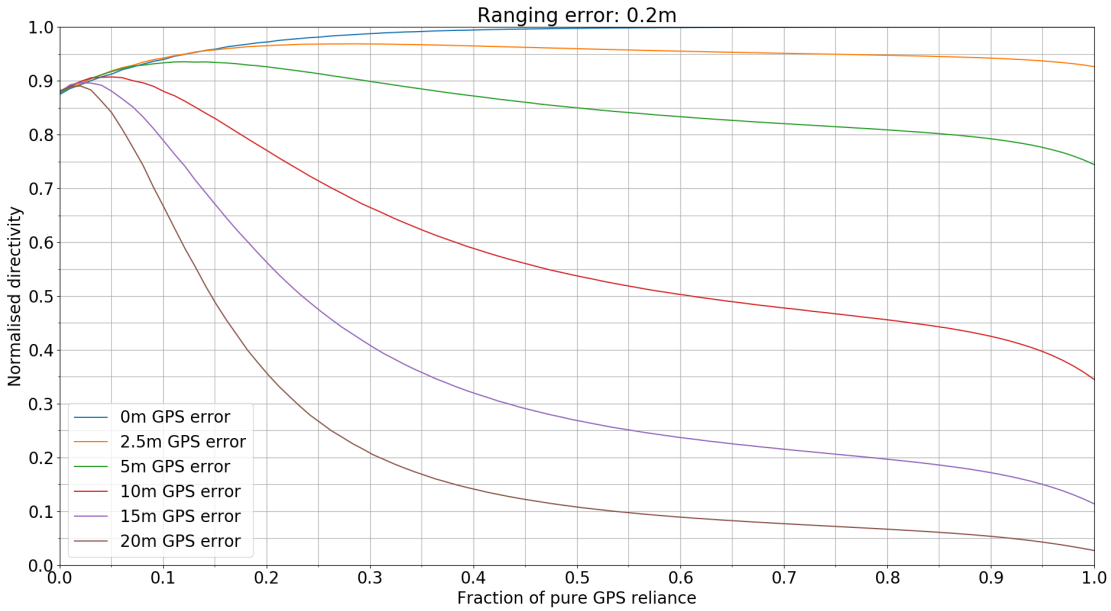

Figure 4.1. *Formation performance vs. reliance on GPS, for an 8 element end-fire array*

A custom formation control algorithm has been described in Section 2.2.1, and specifically in Eqn. 2.2. This makes use of WiFi FTM ranging to enhance the positioning accuracy provided by GPS. The parameters in the formula are α, β, and f. α and β are numerical constants, while f represents the fraction of reliance on GPS. Based on preliminary trials, both α and β were set to 1. Larger values generally result in too large "steps" which cause a node to repeatedly overshoot its destination, while smaller values result in smaller "steps", increasing the time taken to stabilize the formation. Consequently, a value of 1 was found to provide an adequate balance. It should be noted that these constants can and should be optimized for the particular combinations of formation, UAV

hardware, expected positioning errors, and operation time in any future work.

Tests have also been undertaken to find values for f which can together provide an illustrative picture of the behavior of the formation control. In the tests, 4 UAVs have been tasked to maintain a straight line formation. Specifically, the UAVs are to form a horizontal line, with a spacing of $10m$ between each UAV. The performance is measured in terms of the maximum normalized gain of the antenna formed by the formation, as per the work in [7]. The errors in GPS-reported position, and in ranging-reported distances are varied, as is the amount of reliance on GPS. It was found that the effects of variations in ranging errors were negligible, as long as the values were within realistic bounds. Consequently, the tests have focused on the GPS errors and the value of f.

The GPS-reliance (f), as mentioned, is a fraction, where a value of 1 means FTM is not used, i.e. only GPS-reported position is used to build the formation; while a value of 0 means that the UAV does not take into consideration its ideal position, but instead places more importance on having correct distances to its neighbors. The results, which can be seen in Fig. 4.1 indicate that an f value of 0.3 has superior performance for the expected error ranges, while also providing some leeway in case of worse GPS working. This is therefore selected as one of the values of f to be investigated, along with 0.6 and 1, to altogether obtain a representative spread.

Antenna selection

As part of the postprocessing, the antenna element mounted on each individual UAV needs to be defined. Stemming from the nature of the work of this thesis, there are a few constraints that affect the choice of an appropriate antenna. The first is the operating wavelength, which is in the order of tens of meters. To avoid a loss of efficiency, the requirement for relatively large antennas (multiple meters) comes up. The second, conflicting constraint has come from the fact that the antenna needs to be small enough to be mounted on a highly mobile UAV.

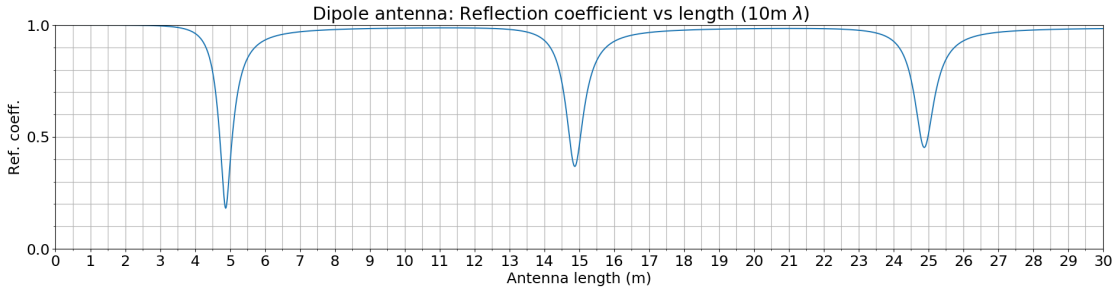

Figure 4.2. *Reflection coefficients for dipole antennas at $10m$ wavelength*

The fact that the efficiency of an antenna is inversely proportional to the reflection coefficient of an antenna [3] has been used to evaluate the efficiency of the antennas. In the case of simple dipole antennas, a wavelength of $10m$ results in the need for a $5m$ antenna, as can be seen in Fig. 4.2. The radiation pattern for this antenna, pictured in Fig.

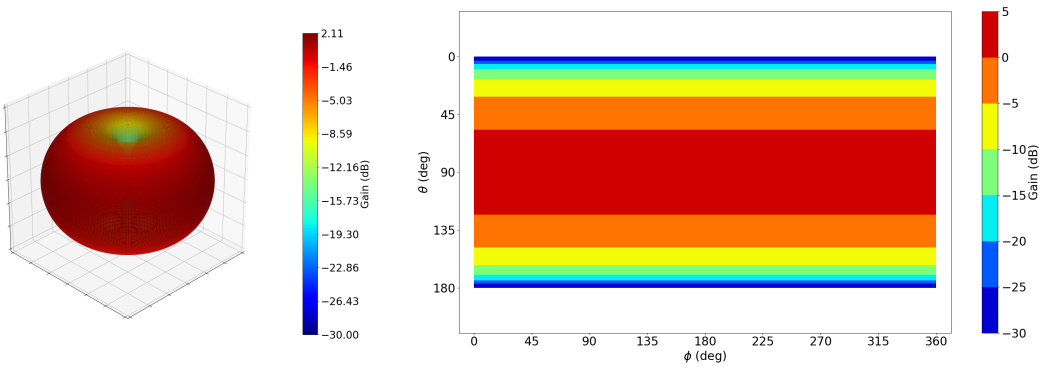

(a) *3D radiation pattern*

(b) *Contour plot*

Figure 4.3. *Radiation pattern for a $5m$ dipole antenna*

4.3, clearly depicts an omnidirectional pattern, with a dip in the gains along the axis of the antenna. This presents an acceptable solution in terms of the pattern alone, however the size of the antenna renders it unsuitable for convenient placement on a UAV.

In an effort to reduce the physical bounds of the antenna, the antenna shape is then changed to that of a coil antenna, visualized in Fig. 4.4a. The reflection coefficients for some different possible configurations have been examined, with the results shown in Fig. 4.4b. Unfortunately, all the antennas with low reflection coefficients (e.g. single loop at $1.6m$ radius) turn out to be too large for mobile operation.

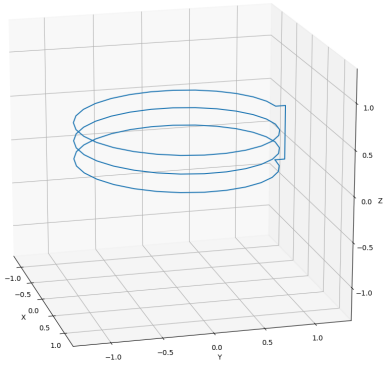

(a) *A coil antenna with 3 loops*

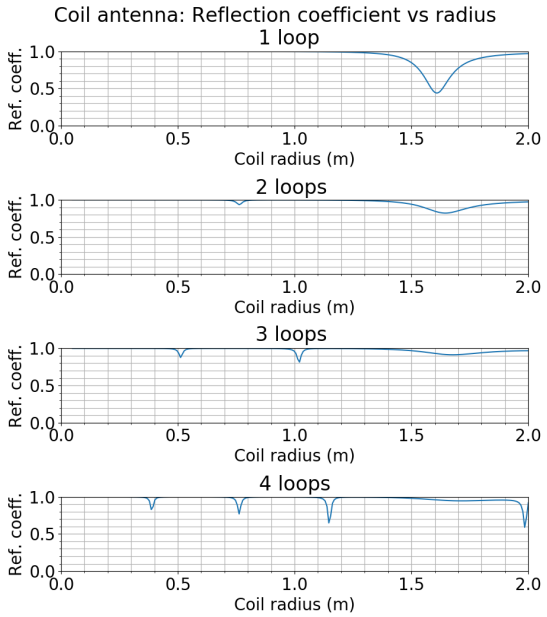

(b) *Reflection coefficients for coil antennas*

Figure 4.4. *Structure and reflection coefficients for coil antennas*

Since there is a need to pack still larger lengths of antenna into smaller spaces, the option considered next is to add "indents" into the coil, in effect making it "star"-shaped. The reduction factor of the radii of the indent points compared to the larger outer radius

is now referred to as the indent factor. Fig. 4.5 presents one such antenna with 28 individual straight segments and an indent factor of 0.5. The reflection coefficients for a variety of such "star" antennas have been generated, and are shown in Fig. 4.7. Both the number of segments and the number of loops have been varied, and the results indicate that a "star" shaped antenna with a single loop and around 0.5 indent factor has a local maximum of efficiency at around $0.9m$ radius while also having a somewhat manageable size.

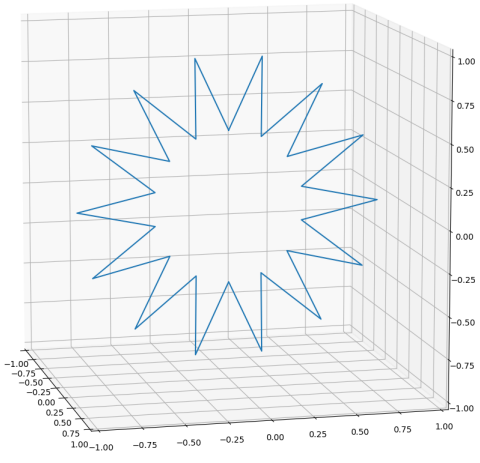

Figure 4.5. *A "star"-shaped antenna with a single loop and 28 segments*

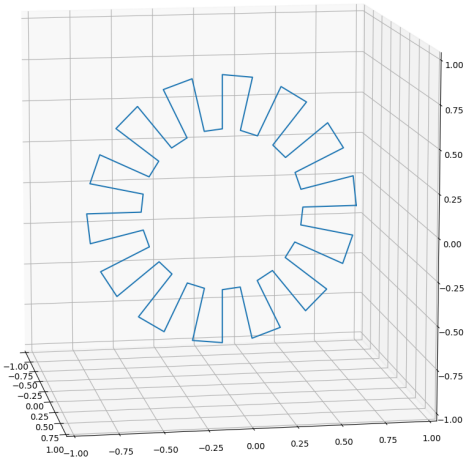

Figure 4.6. *A meander antenna with a single loop and 28 "meanders"*

In order to further reduce the size, meander antennas are next considered. Specifically, meanders have been added to the loops of a coil antenna the same way that indents have been added in the case of the "star" antennas. An example of a meander antenna with 28 "meanders" and an indent factor of 0.6 is shown in Fig. 4.6. The reflection coefficients of such meander antennas for variations in the number of loops and the indent factor are depicted in Fig. 4.8. An examination of these results reveals two interesting candidates: single loop with 28 "meanders", indent factor 0.6 and $0.79m$ radius, or a single loop with indent factor 0.5 and $0.71m$ radius. The former has a somewhat better efficiency at the cost of slightly larger size. The particular choice then depends on the circumstances of the application, but the former can be considered sufficient.

The radiation pattern for the selected antenna candidate, i.e. the meander antenna with 28 "meanders", an indent factor of 0.6 and a radius of $0.79m$ is shown in Fig. 4.9. This shows an almost omnidirectional pattern, highly similar to that of the dipole. One issue with this antenna, specific to simulations with NEC2, is that the larger number of individual straight line segments results in longer computation times. Dipole antennas on the other hand, have a much simpler structure and result in notably lower computation times while having almost the same radiation pattern. As a result, for practical reasons further simulations make use of an electrically small dipole $0.5m$ in length as the antenna element mounted on the UAVs.

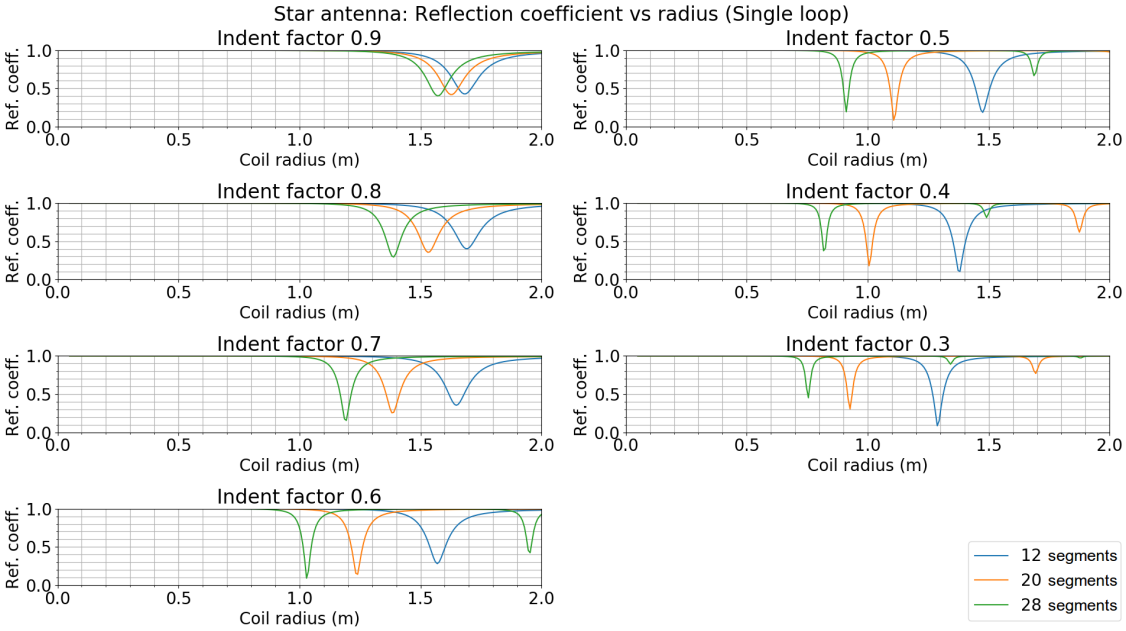

(a) *Variation over number of segments*

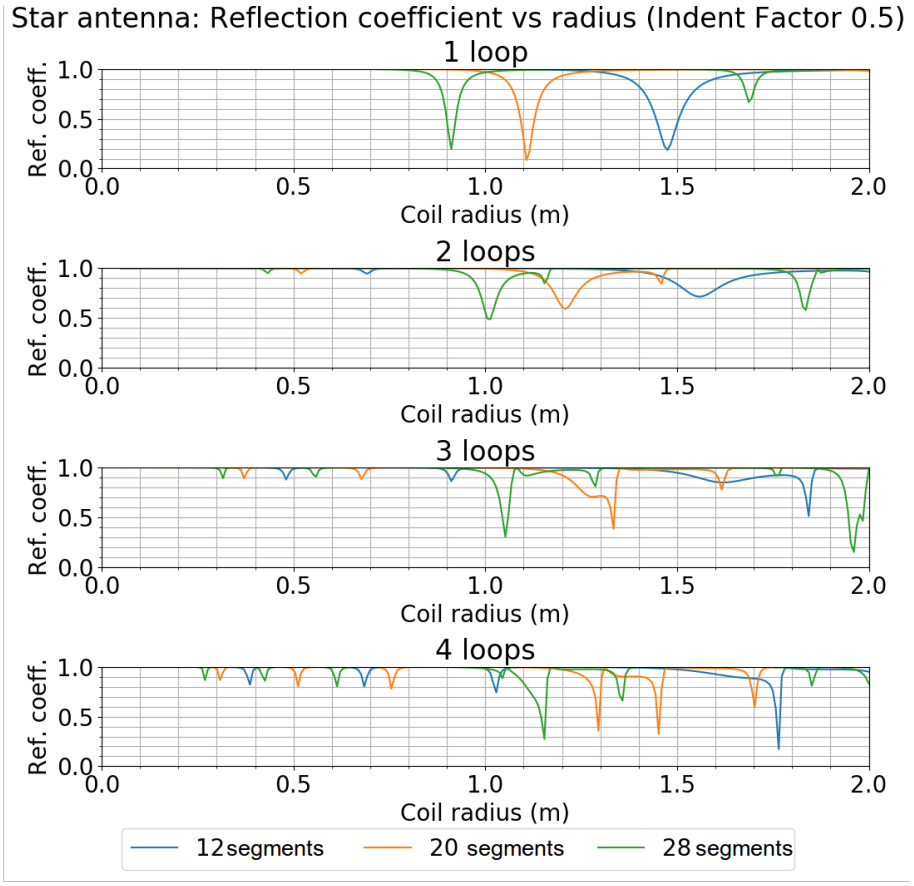

(b) *Variation over number of loops*

Figure 4.7. *Reflection coefficients for "star" antennas*

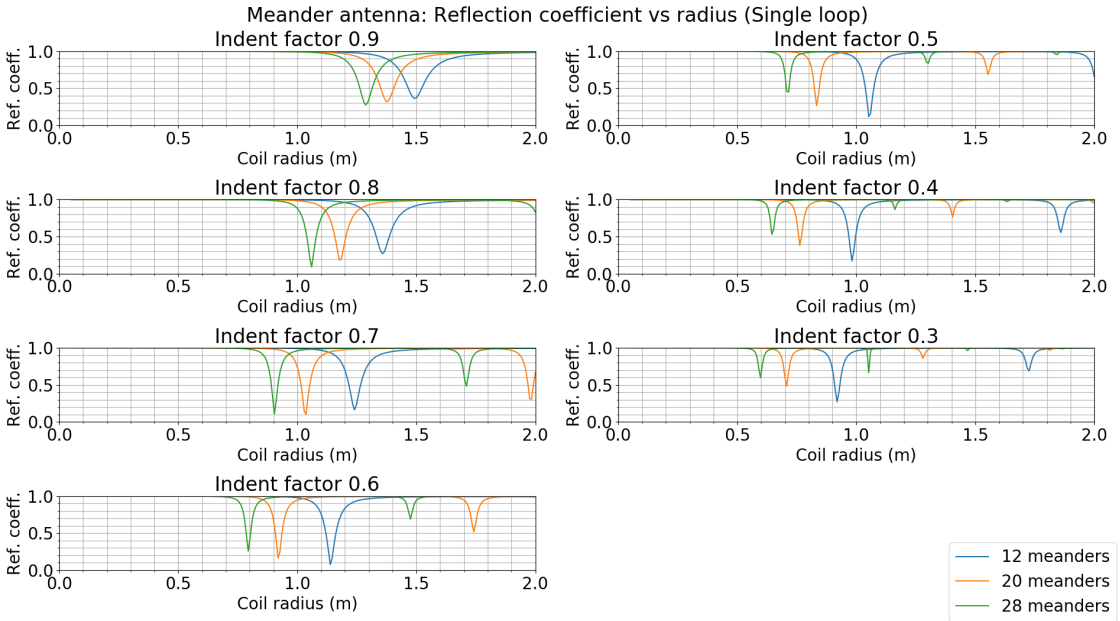

(a) *Variation over number of "meanders"*

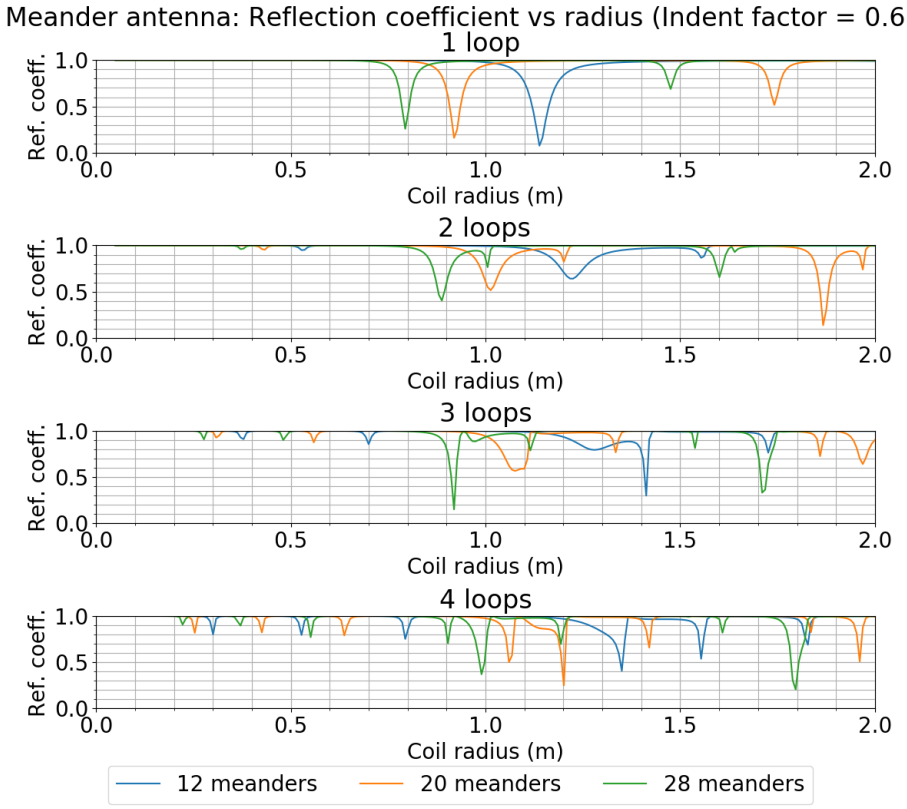

(b) *Variation over number of loops*

Figure 4.8. *Reflection coefficients for meander antennas*

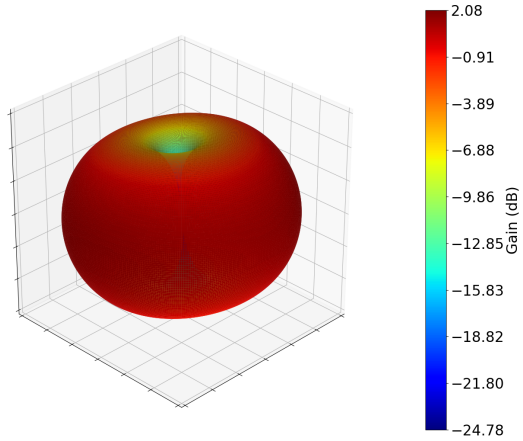

(a) *3D radiation pattern*

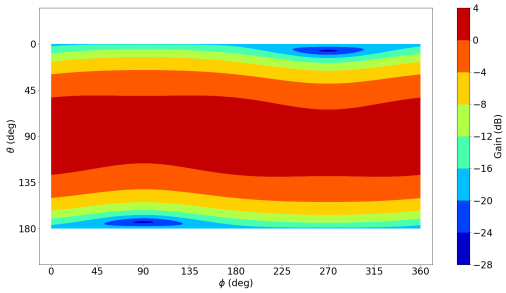

(b) *Contour plot*

Figure 4.9. *Radiation pattern for a meander antenna with indent factor* 0.6 *and radius* $0.79m$

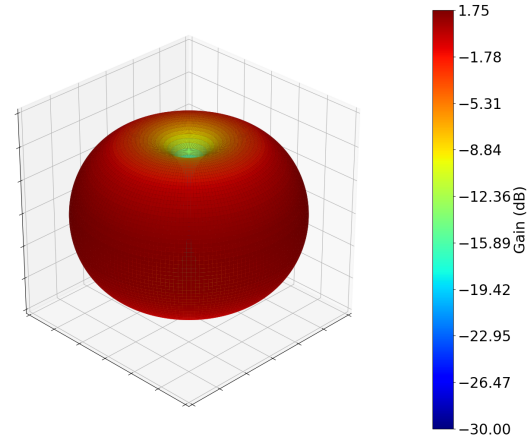

(a) *3D radiation pattern*

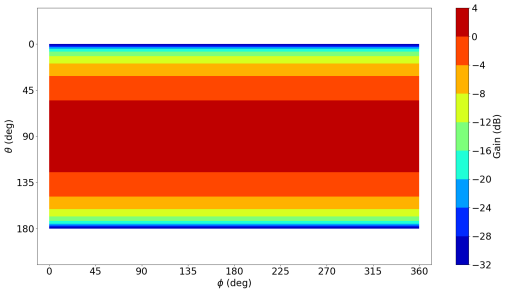

(b) *Contour plot*

Figure 4.10. *Radiation pattern for a* $0.5m$ *dipole antenna*

4.2 Effects of Formation Shape and FTM Usage

Having selected the antenna elements, the next step of the methodology, as laid out previously, is to examine the performance of different formations and formation control parameters. The Maximum gain (in dB), and the difference in gain between the main and side lobes for the various considered formations are presented in Table 4.1, while the 3D radiation patterns are illustrated in Fig. 4.11.

It should be kept in mind that the formations have been selected specifically to take advantage of supergain effects. Further, the aim has been to select a sufficiently well performing formation; the selection of a truly optimal formation for a given task and number of UAVs is out of the scope of this work and is a potential problem for future efforts. Additionally, in the case of the formations with 3x3 elements, the gain can be expected to be slightly higher than the others due to a larger number of elements, but evidently (as is clearly visible in Table 4.1) the effects of different formations are more significant – the highest gain is from an 8-element formation, not 9.

Before diving into the results it is important to note certain conditions that are implicitly enforced on the collection of processable results from the simulations. The first is that the collection of UAV positions and orientations begins only when the RMS of position errors is below a user-defined limit ($0.5m$ in this case). The second condition is introduced through the automated detection of the main lobe of the radiation pattern. In case of an absence of a clearly defined main lobe (defined as a sufficiently convex bounding contour on a 2D contour map of the radiation pattern), the postprocessing is aborted. In effect, high instability in a formation, resulting in high position errors or in the actual absence of a main lobe, precludes it from successful processing and analysis.

Each of the selected formations has been tested with a wavelength of $10m$, and a wind force strength of $2N$. The results from these tests can be seen in Figs. 4.12, 4.13, and 4.14. Particular notable observations from these plots are now identified and discussed.

Overall, the angular deviations displayed by the different formations are lower than what might be intuitively expected, with the deviations for most formations almost always being below $3°$. When comparing the angular deviations between the different formations, one

Formation	Max Gain (dB)	Gain difference – main & side lobe (dB)
1x8 element end-fire	9.73	16.43
2x4 element end-fire	11.02	6.99
3x3 end-fire (triangle)	11.95	5.93
3x3 end-fire (flat)	12.25	8.61
4x2 end-fire (square)	11.60	2.95
4x2 end-fire (flat)	13.26	8.38

Table 4.1. *Ideal positioning metrics for the considered formations (λ: $10m$)*

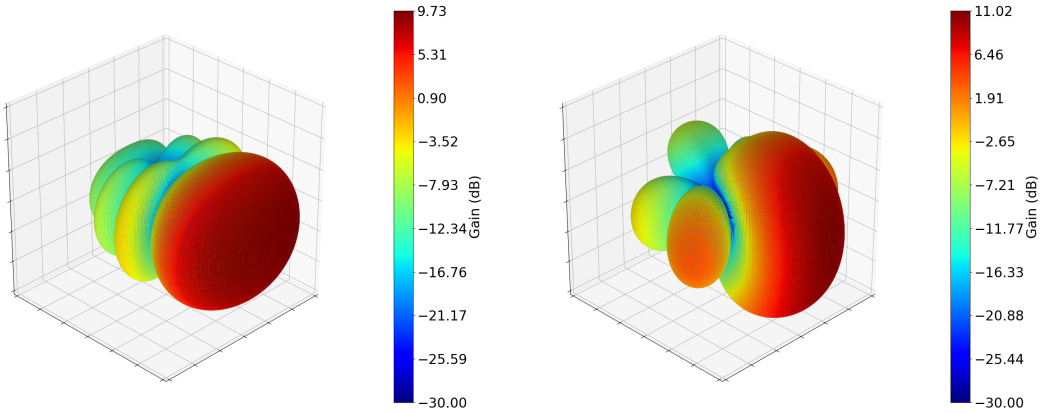

(a) *1x8 element end-fire* ***(b)*** *2x4 element end-fire*

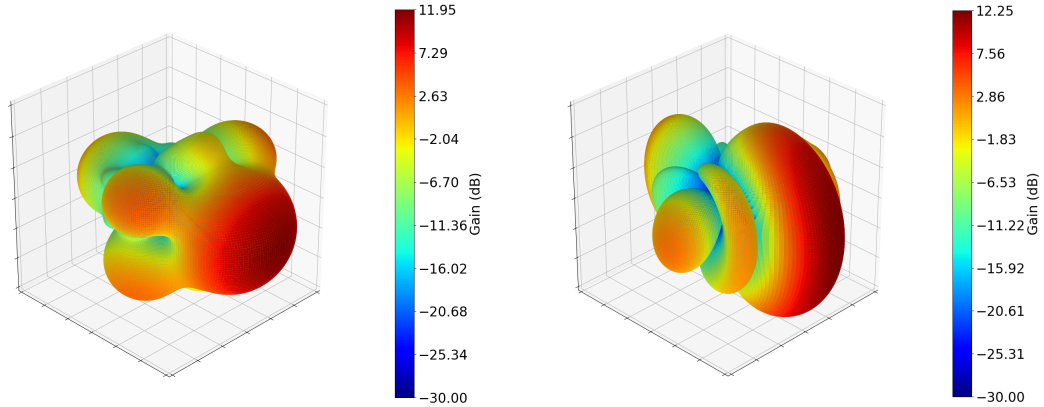

(c) *3x3 end-fire (triangle)* ***(d)*** *3x3 end-fire (flat)*

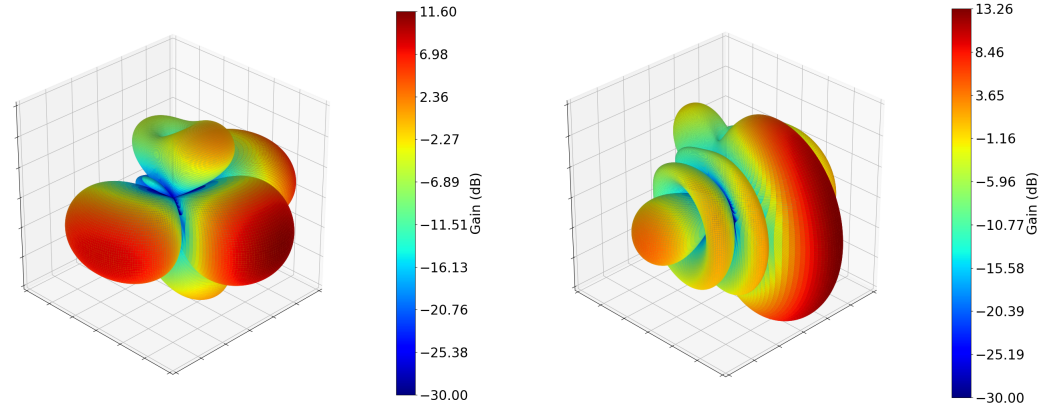

(e) *4x2 end-fire (square)* ***(f)*** *4x2 end-fire (flat)*

Figure 4.11. *Antenna radiation pattern for various formations*

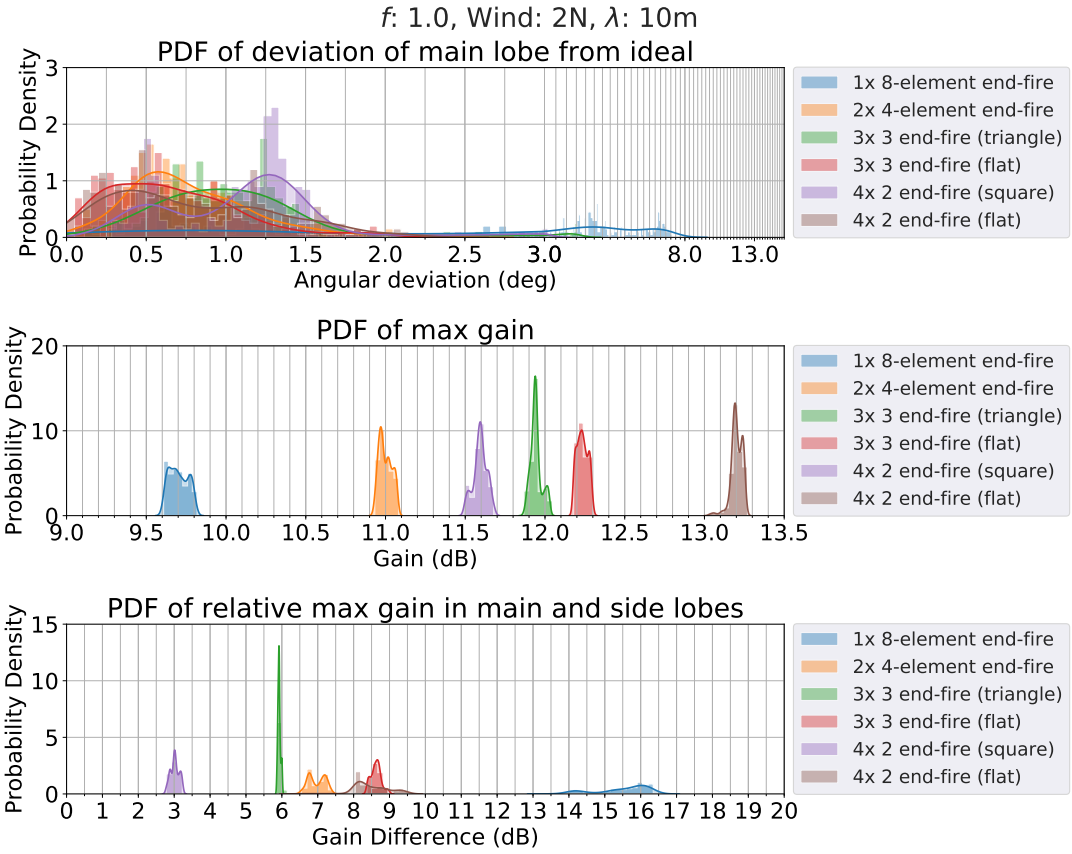

Figure 4.12. *Results for formation variation with* $f = 1$

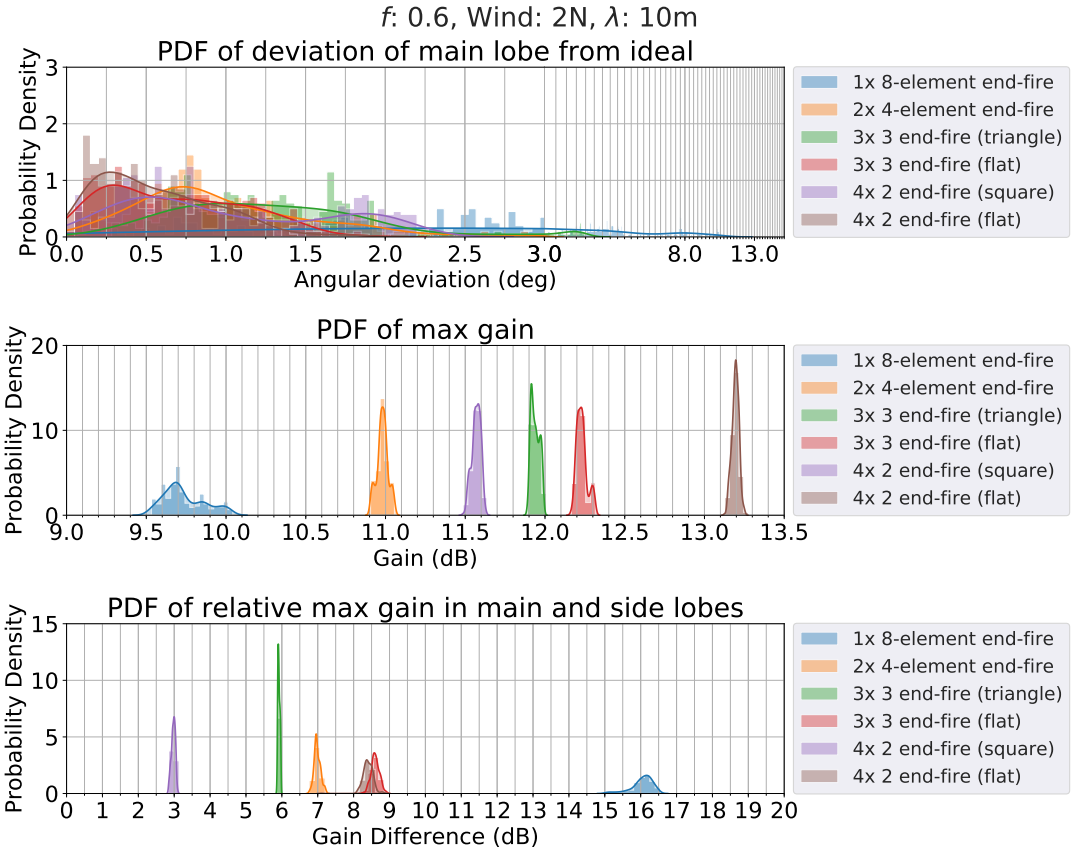

Figure 4.13. *Results for formation variation with* $f = 0.6$

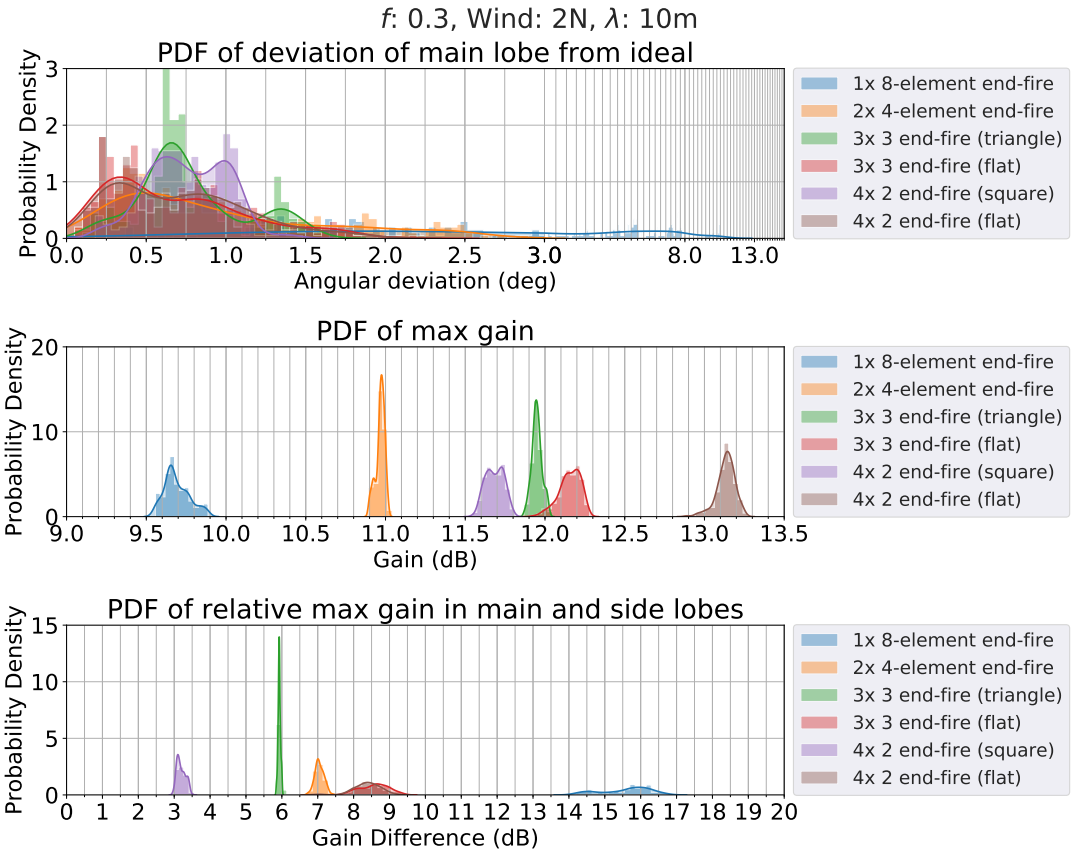

Figure 4.14. *Results for formation variation with* $f = 0.3$

clearly visible outcome is that the "flat" formations (shown in red and brown in the plots) consistently have lower deviations compared to that of the others. Within the family of "flat" formations, the size of each individual end-fire seems inversely related to the amount of deviation; e.g. the 4x2 has lower deviation than the 3x3, which in turn outperforms the 2x4, with the 1x8 having in all cases the highest deviations of any of the tested formations.

One notable observation regarding the angular deviations displayed by the non-"flat" formations, i.e. the 3x3 (triangle), and the 4x2 (square), is that they are able to leverage the benefits of FTM-based positing to a greater extent, i.e. for increasing values of f, the deviations reduce. The gain is more prominent in the case of the 4x2 (square), which lags behind the 3x3 (triangle) for $f = 1$ and 0.6, but arguably has better accuracy in the $f = 0.3$ case. This suggests that formations that are more "rolled up" might tend to see better performance gains from the usage of FTM data. A concrete conclusion of this nature would however need a targeted study with a larger variation of formation shapes.

The value of the maximum gain shows a very direct dependence on formation shape, which is seen in the clear separations between the distributions of the maximum gain for the different formations. The highest gain is consistently provided by the 4x2 (flat) formation at around $13dB$, with the next highest being the 3x3 (flat) at around $12dB$. It is interesting to note the difference between the two mentioned flat formations, despite the 3x3 having one element more than the 4x2 and a very similar configuration. This suggests

that the supergain advantages from a longer front-fire array are more significant, which is in line with the observations in [36].

The maximum gains are therefore clearly in agreement with the predicted maximum gains for no position errors (shown in Table 4.1). Accordingly, the next best performing formations are the 3x3 (triangle), and the 4x2 (square), which have multiple shorter front-fires (specifically one for each pair) compared to the flat formations. These are followed by the single 1x8 end-fire which has a gain slightly over 9.5dB. This is interestingly somewhat against the expectation to see large supergain effects from having smaller spacing between the elements, as described in [36]; this finding presents another area for future work to focus upon.

The maximum gain shows a much smaller variation than the angular deviation across the different values of f. The only visible change is that there is a marginal increase in the "spread" (i.e. the variance) of the probability distributions for a few of the formations (e.g. 4x2 (flat), 3x3 (flat), and 4x2 (square)); however, the opposite change is visible for the 2x4 formation, which becomes "sharper" for $f = 0.3$. These contradictory trends lessen the certainty of any conclusions drawn regarding the effect of FTM on gain variance.

Similar to the case of the maximum gain, the difference between the maximum gains in the main and side lobes shows a very clear dependence on the formation used. These distributions moreover do not deviate much from the baseline values in Table 4.1. It is also helpful to note the radiation patterns depicted in Fig. 4.11 which clearly make the side lobe structures visible, providing the appropriate context for the results obtained.

The single 1x8 end-fire has, as expected, the largest difference between the main and side lobes. However, it also has the highest variance of the tested formations, a fact that can then be connected to the corresponding spread out distribution of angular deviations. There is then a large gap, of around $5dB$, before the next formations are encountered, which are the two flat formations, the 3x3 and the 4x2. There is interestingly very little difference between the distributions for these two formations, especially considering the large gap between their maximum gains, and the difference in the number of UAVs needed.

The next in line are as expected the 2x4 end-fire, the 3x3 (triangle), and the 4x2 (square). The 2x4 unsurprisingly has virtually the same distribution shape as the two other flat formations. However, the 3x3 notably has the sharpest distribution of all the formations. This is interesting to note especially when also considering the lack of any similar distinguishing sharpness in the angular deviation. This suggests that the 3x3 (triangle) is possibly in a sense more "rigid", maintaining relative positioning despite deviations in orientation of the entire structure. The lack of a similar degree of sharpness in the case of the 4x2 (square) hints at the sharpness not simply being a result of a 3 dimensional structure.

Changing the reliance on GPS (f), similar to the case of maximum gain, has very little evident effect on either the magnitudes of the relative gain between main and side lobes, or their distributions. The case with $f = 0.3$ in particular shows a small increase in

variance compared to the other cases, which can therefore be deemed to be the cost for the simultaneous reduction in the angular deviations observed.

Candidate Configuration Selection

As it is required to select a single candidate formation for the next stage of the simulations, the characteristics of the performance of the tested formations and variations of FTM reliance are now compared.

The 1x8 end-fire has by far the smallest side-lobes, although this comes at a cost of the lowest gain, and the highest angular deviation. This makes it a good choice for cases where having small side lobes is critical and gain is not the central consideration. The 2x4 formation shows an average to low performance in all categories.

In terms of gain and deviations, both the 3D formations (i.e. the 3x3 (triangle) and 4x2 (square)) are right in the middle of the different formations, while being at the lower end in terms of side-lobe-relative gain. The 4x2 has the worst performance of all tested formations in terms of side-lobes, while performing slightly worse than the 3x3 in terms of gain and deviations. It is however one of the only formations to have no back-lobe, making it an acceptable choice where a central consideration is the absence of radiation in a direction directly opposite the intended direction.

The 3x3 (triangle) as mentioned has a higher gain and lower deviations than the 4x2 while retaining smaller side-lobes. It additionally has the distinction of having the most consistent side-lobes. This can be an important factor in some applications, where precise compensations are made for the interference from the side-lobes of neighboring antenna elements.

The 3x3 (flat) and 4x2 (flat), on the other hand are the highest in terms of gain, while consistently having the lowest deviations; their side-lobe-relative gains are second only to the 1x8. The 4x2 (flat) specifically, has by far the highest gain of all, while also showing performance equivalent to the 3x3 (flat) in terms of side-lobe-relative gain and angular deviation, despite the latter having 1 antenna element more.

In consequence, the 4x2 (flat) emerges as one of the better-performing formation candidates for synthesizing an antenna out of a swarm of UAVs in the general case. It should be noted that one of its potential downsides is related to the fact that this formation has one of the largest end-to-end sizes; specifically $0.85 \cdot \lambda \cdot \frac{n}{2}$, where n is the number of UAVs in the formation. For larger formations, this might be impractical due to space restrictions, and if large enough, the distance between the furthest UAVs might be too large for communication. Accordingly, the choices made for a formation of a different scale can be expected to be different.

When comparing the results for different values of f, there are two main points that stand out. Firstly, the angular deviations for $f = 0.3$ are in general lower than for $f = 0.6$ and 1;

this effect is especially strong in the case of the 3D formations (i.e. the 3x3 (triangle) and 4x2 (square)). Secondly, for the maximum gain and the side-lobe-relative gains, there is little change in the magnitudes, but there is a slight increase in variance for a few of the formations. Although the specific circumstances of each application case require different priorities, on the whole it might be judged that the improved accuracy makes up for small additional variance in the maximum gain and side lobe levels.

An additional observation supporting a lower f comes from the results in Fig. 4.1, which suggest that lower f makes formations more resilient to GPS errors. As a result, a configuration of a 4x2 (flat) formation with an f value of 0.3 is chosen to be the candidate for further investigation.

4.3 Effects of Wavelength and Wind Strength

Having selected a well performing configuration, the next task is to investigate the effects of changes in wavelength and wind strength on the performance of the formations in terms of the same three metrics used in the previous section. To reiterate, since the formations are scaled based on the operating wavelength, a larger wavelength results in a larger spacing between individual UAVs, while positioning errors can be expected to remain unaffected. Increased mean wind strength on the other hand makes it harder

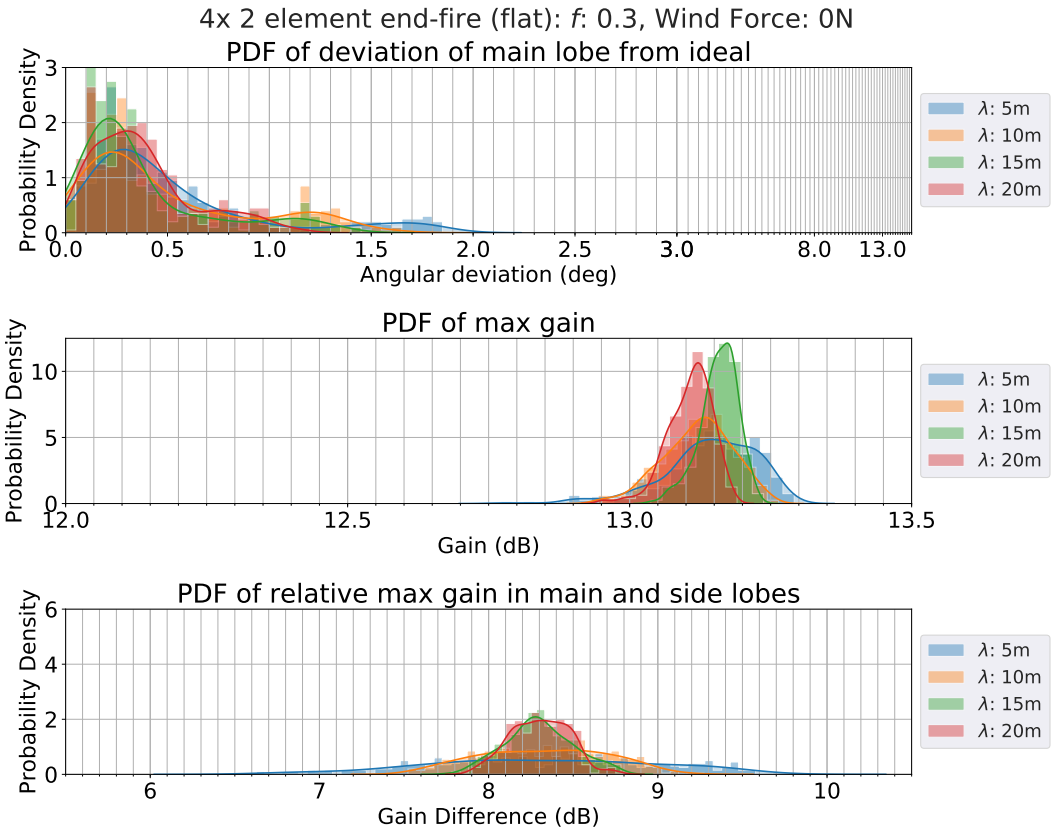

Figure 4.15. *Results for wavelength variation with* $0N$ *wind*

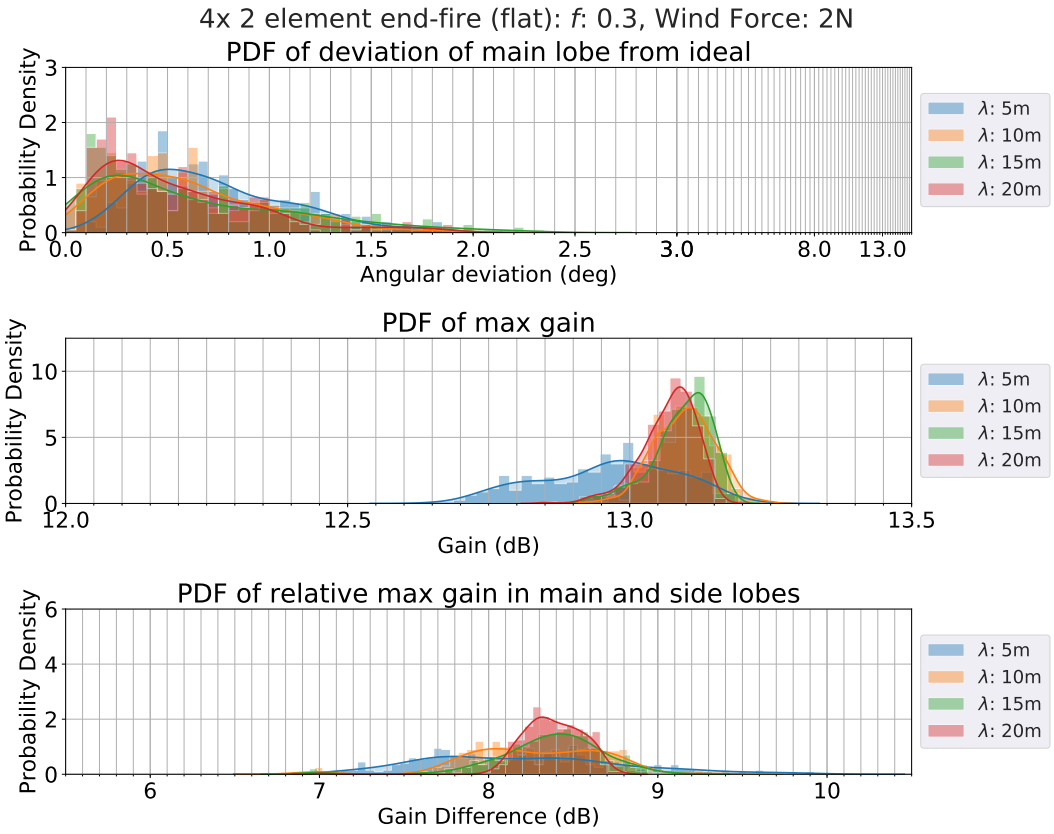

Figure 4.16. *Results for wavelength variation with* $2N$ *wind*

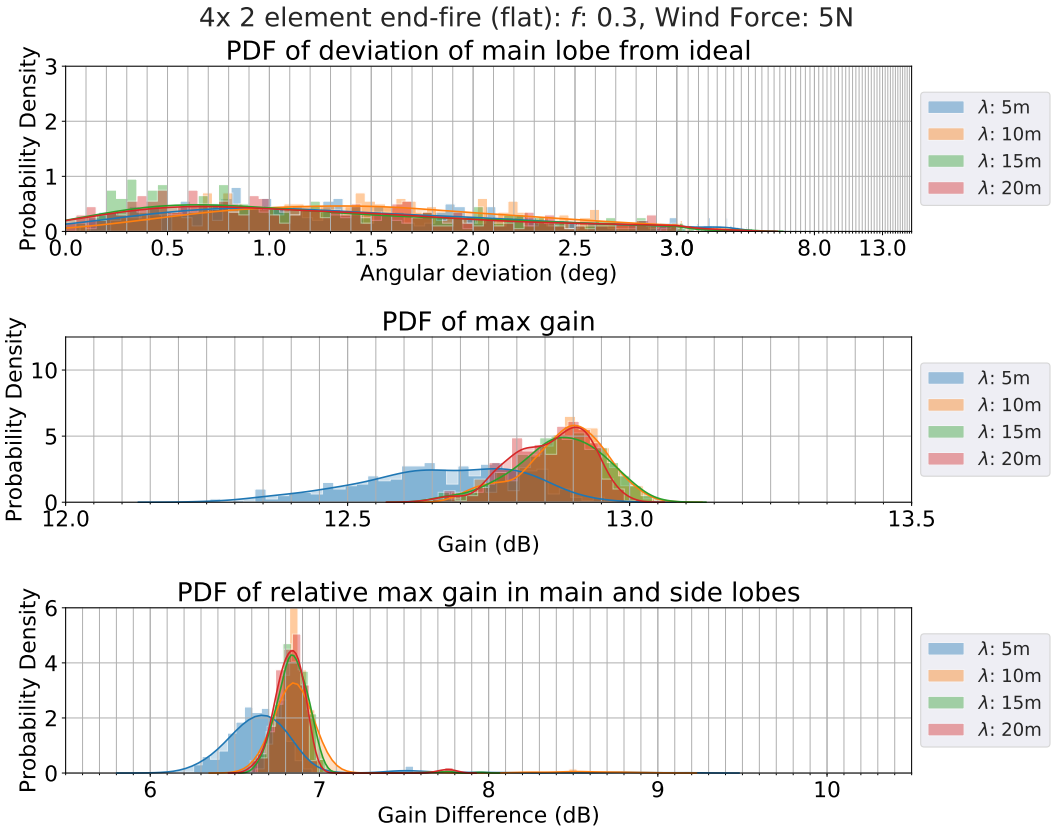

Figure 4.17. *Results for wavelength variation with* $5N$ *wind*

for the UAVs to maintain position and orientation. It is important to note that neither the wavelength nor the wind strength affect either of the expected maximum gain or the side-lobe-relative gain; the effect of both is to only affect formation stability.

The mean wind strengths have been varied over $0N$, $2N$, and $5N$. At high wind strengths ($7.5N$+), the formations usually failed to satisfy the condition imposed upon the collection of data, i.e. having the RMS position error below $0.5m$. Investigation revealed that the high winds interfered with the IMU readings, resulting in inaccurate flight patterns. This corresponds to real-word experiences, where UAVs have trouble flying in high-wind conditions.

The results from the different configurations can be seen in Figs. 4.15, 4.16, and 4.17. Comparing the results across the different wind strengths, there are a number of points that are immediately evident. Firstly, for the $0N$ wind, the angular deviations are very low; the bulk of most of the distributions is under $0.5°$. For the $2N$ wind case, there is an overall increase in the deviations, with the majority now under $1°$ instead. This trend continues, and even intensifies, in the $5N$ case, where there is almost no readily observable "peak" anymore. It is therefore apparent that increasing wind strength effectively results in larger angular deviations.

Next is the case of the maximum gain of the antenna synthesized by the formation. Here too, an increase in the wind strength can be seen to readily reduce the maximum gain. At $0N$ the distributions are in line with the expected ideal positioning gain of $13.26dB$. At $2N$ wind, the bulk of the distributions have visibly reduced by around $0.1 - 0.5dB$. At $5N$ wind strength, the distributions now almost entirely lie below $13dB$, showing almost a further $0.5dB$ reduction in gain. Greater wind strength is therefore directly associated with a reduction in maximum gain.

The third and most dramatic change is seen in the maximum gain difference between the main and side lobes. The results for $0N$ and $2N$ display a very marginal change, with the distributions being close to the ideal value of $8.38dB$. The $5N$ case presents a change of slightly over $1dB$ for the greater part of the distributions, with a small number of samples spread in the 7 to $8.3dB$ range.

One important point to note at this stage is that the procedure employed for automated detection of the main lobe relies on the generation of contours over the gains for the antenna at different angles (see Fig. 4.18). A deformation in the radiation pattern due to position errors therefore changes the precise angular range recognized as the main lobe, which is affected by a configurable contour count/range; i.e. a change in the configuration of the detection algorithm can be expected to change the results. However the fact remains that a reduction in the reported side-lobe-relative gains is a result of a reduction in the "actual" side-lobe-relative gains. In this manner, a clear inference can be drawn about the reduction in side-lobe-relative gains with an increase in wind strength.

The effect of a variation in wavelength also demonstrates discernible trends. Both the $15m$ and $20m$ wavelength cases indicate clear advantages over the $10m$ case. These

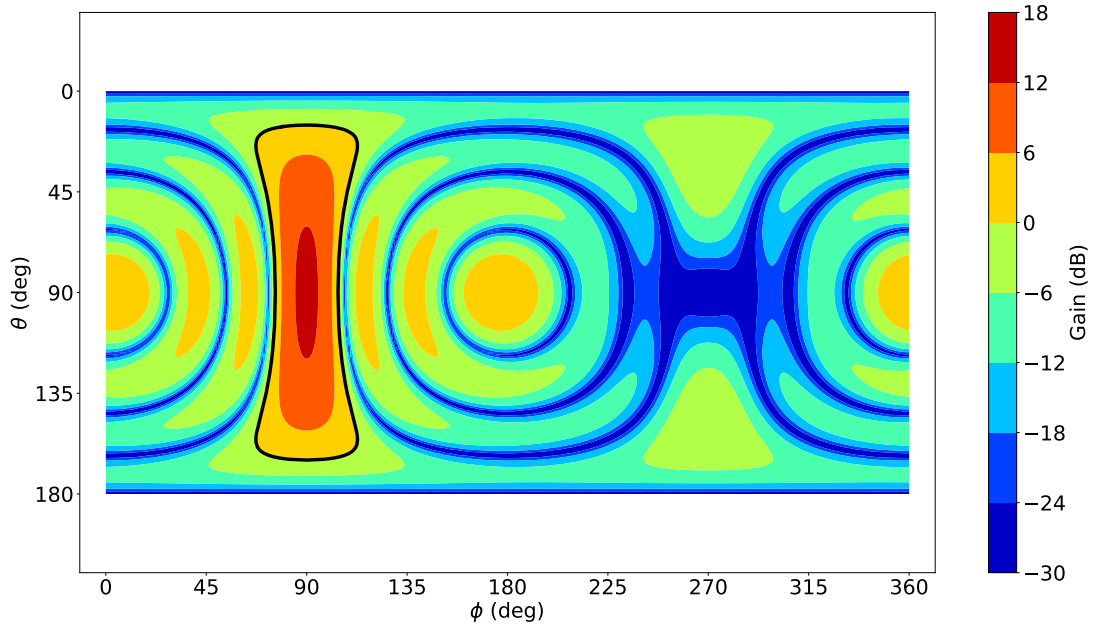

(a) *Radiation pattern for ideal positions*

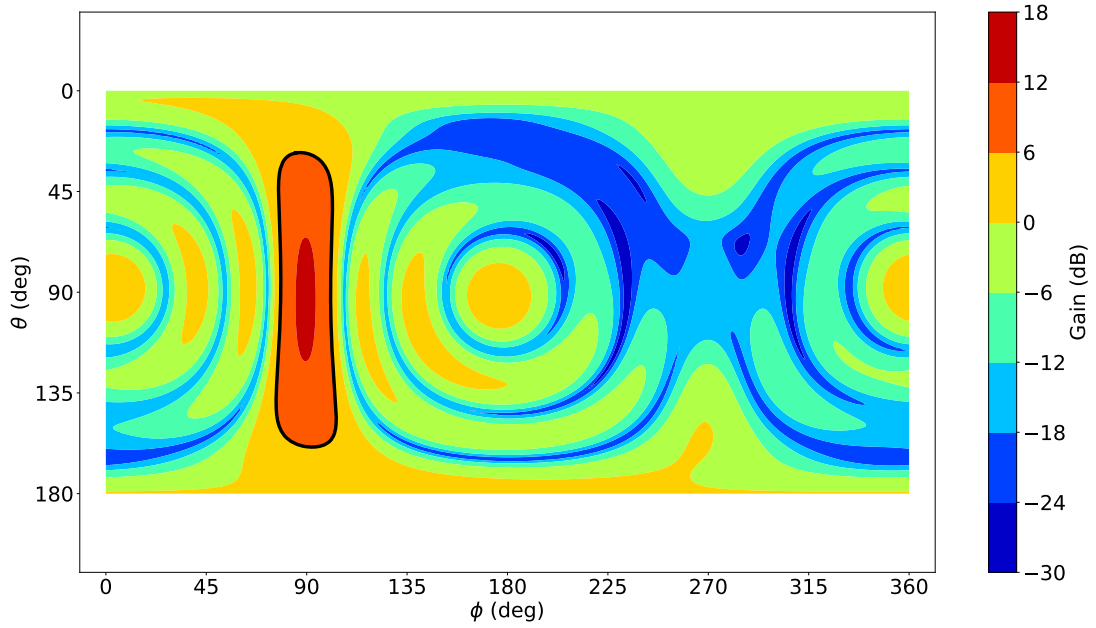

(b) *Radiation pattern for simulated positions*

Figure 4.18. *Radiation pattern comparison for an ideal and simulated 4x2(flat) antenna,* $\lambda = 10$*, wind strength* $5N$*. Detected main lobe outlined in black.*

advantages are seen not in the magnitudes of the distribution, but rather in a decreased variance; i.e. the $10m$ case shows greater instability for the same wind strength compared to 15 and $20m$. This gap widens further in the case of the $5m$ wavelength, which consistently and unambiguously fails to achieve the performance of the larger wavelengths, both in mean and variance. This is best seen in the maximum gain for the $2N$ and $5N$ wind cases, and in the side-lobe-relative gains in all three plots.

Consequently, the inference can be made that larger wavelengths (leading to larger formations) are expected to increase stability and performance in terms of the selected metrics. Similarly a conclusion about increased wind strength negatively affecting antenna performance in terms of all the selected metrics can be drawn.

5 CONCLUSION

This chapter aims to sum up the results of the work carried out for this thesis, while at the same time reflecting on various aspects of the study. Further, possibilities for future work that extend the work presented here are discussed, finally closing with a clear description of the main contributions of this work.

The results from the simulations carried out have been presented in Chapter 4. The findings indicate that the formation shape is one of the most crucial factors affecting the antenna performance. It is especially encouraging to note that an attempt to leverage high-efficiency supergain effects does indeed result in better antenna performance. Additionally, for a number of UAVs capped at 10, 2D formations tend to result in overall better performance followed by more rigid 3D formations. Traditional linear end-fire formations on the other hand have the upside of small side-lobes. This suggests that formation, like the other parameters, be chosen based on the requirements of the target application.

The usage of inter-element distance estimates (FTM ranging) to improve positioning accuracy has shown to generally be a worthwhile undertaking, given the presence of non-trivial GPS errors. Placing high weightage on GPS unsurprisingly limits performance based on GPS errors; increasing inter-element spacing weightage (under the tested conditions) generally improves performance. Interestingly, but also somewhat expectedly, more rigid 3D formations benefit from the use of inter-element spacing more than their 2D counterparts.

The effects of changes in operating wavelength and wind strength are generally as expected. Larger wavelengths result in overall better performance by increasing the effective positioning accuracy, since deviations evidently do not scale with inter-element spacing. Similarly, higher wind strengths result in lower performance, since wind forces directly act to increase position/orientation deviations; additional orientation deviations are observed due to a counter-tilt as the UAVs attempt to fly against the wind.

The methodology in this thesis has been designed to be capable of accurately studying changes in the behavior of a swarm of UAVs in a holistic manner. The different aspects involved in this behavior (physical, robotics, communications, electromagnetics) are each handled by a dedicated tool, with the overall structure allowing for flexibility in the study of the effects of various parameters. The results generated in this work have generally been in line with expectations, while also highlighting certain interesting trends. This builds faith in the validity and merit of the chosen methodology.

Future efforts that aim to expand upon the work in this thesis can focus on one of two main branches: a further investigation of the performance of swarm-based Synthetic Aperture Antennas; or an expansion of the robustness of the methodology (and therefore also of the simulation platform) used. Tasks that can be undertaken in the former are, for example: development of a more flexible and better performing formation control algorithm; a much more in-depth study of different possible formations, especially ones making use of a much larger number of elements; and an investigation into the possibilities of leveraging supergain effects in a more effective manner – i.e. achieving performances closer to the theoretical limits. The latter can instead focus on: implementing more accurate ray casting while also supporting diffraction effects; completing the calibration of the ray-casting algorithm with real-world measurements; and on adding support for a more elaborate and realistic wind model within Gazebo.

The contributions of the work in this thesis fall broadly into two categories: the new insights into the operation of swarm-based Synthetic Aperture Antennas; and the newly developed methodology and accompanying simulation platform. In the first, as mentioned above, the understanding of the effects of various parameters has been broadened – these insights are useful for the planning and optimization of any undertakings making use of swarm-based Synthetic Aperture Antennas; this is in addition to the direct increase in theoretical understanding of the performances of such systems. In the second, the developed methodology displays the ability to be flexibly used to investigate a variety of aspects of the behavior of a swarm of UAVs. Finally, the validity of the designed methodology has been demonstrated though the specific study contained in this thesis, making its prospective future applications all the more promising.

REFERENCES

[1] *3GPP TR 25.996 V9.0.0 (2009-12) Spatial channel model for Multiple Input Multiple Output (MIMO) simulations (Release 9)*. 25.996. 3GPP. 2009.

[2] D. Altdorff, N. Schliffke, M. Riedel, V. Schmidt, J. van der Kruk, H. Vereecken and J. Stoll. UAV-borne electromagnetic induction and ground-penetrating radar measurements: a feasibility test. *Water Resour Res* 42 (2014), W11403.

[3] C. A. Balanis. *Antenna theory: analysis and design*. John wiley & sons, 2016.

[4] O. Bimber, I. Kurmi, D. C. Schedl and M. Potel. Synthetic Aperture Imaging With-Design of UAVs-Based 3D Antenna Arrays for a Maximum Performance in Terms of Directivity and SLL Drones. *IEEE computer graphics and applications* 39.3 (2019), 8–15.

[5] C. A. Boano, H. Wennerstrom, M. Zuniga, J. Brown, C. Keppitiyagama, F. Oppermann, U. Roedig, L.-Å. Norden, T. Voigt and K. Römer. Hot Packets: A systematic evaluation of the effect of temperature on low power wireless transceivers. (2013).

[6] S. Breheny. Design of a four-rotor autonomous helicopter for vehicle-based phased antenna arrays. (2007).

[7] S. H. Breheny, R. D'Andrea and J. C. Miller. Using airborne vehicle-based antenna arrays to improve communications with UAV clusters. *42nd IEEE International Conference on Decision and Control (IEEE Cat. No. 03CH37475)*. Vol. 4. IEEE. 2003, 4158–4162.

[8] A. Camps, M. Vall-Llossera, I. Corbella, F. Torres and N. Duffo. Angular and radiometric resolution of Y-shaped nonuniform synthetic aperture radiometers for earth observation. *IEEE Geoscience and Remote Sensing Letters* 5.4 (2008), 793–795.

[9] G. Carneiro. NS-3: Network simulator 3. *UTM Lab Meeting April*. Vol. 20. 2010, 4–5.

[10] R. S. Chandra, S. H. Breheny and R. D'Andrea. Antenna array synthesis with clusters of unmanned aerial vehicles. *Automatica* 44.8 (2008), 1976–1984.

[11] S. Chandrasekharan, K. Gomez, A. Al-Hourani, S. Kandeepan, T. Rasheed, L. Goratti, L. Reynaud, D. Grace, I. Bucaille, T. Wirth et al. Designing and implementing future aerial communication networks. *IEEE Communications Magazine* 54.5 (2016), 26–34.

[12] J. W. Cheong, B. Li, A. G. Dempster and C. Rizos. GPS/WiFi real-time positioning device: An initial outcome. *Location Based Services and TeleCartography II*. Springer, 2009, 439–456.

[13] J. Colorado, M. Perez, I. Mondragon, D. Mendez, C. Parra, C. Devia, J. Martinez-Moritz and L. Neira. An integrated aerial system for landmine detection: SDR-based ground penetrating radar onboard an autonomous drone. *Advanced Robotics* 31.15 (2017), 791–808.

[14] T. Cuvelier and R. W. Heath. Mmwave MU-MIMO for aerial networks. *2018 15th International Symposium on Wireless Communication Systems (ISWCS)*. IEEE. 2018, 1–6.

[15] D. J. Daniels. Ground penetrating radar. *Encyclopedia of RF and Microwave Engineering* (2005).

[16] G. Dhandapani and A. Sundaresan. Netlink Sockets, Overview. *Information and Telecommunications Technology Center, Department of Electrical Engineering & Computer Science, The University of Kansas* (1999).

[17] G. Fasano, A. Renga, A. R. Vetrella, G. Ludeno, I. Catapano and F. Soldovieri. Proof of concept of micro-UAV-based radar imaging. *2017 International Conference on Unmanned Aircraft Systems (ICUAS)*. IEEE. 2017, 1316–1323.

[18] P. Ferguson, F. Busse and J. How. Navigation performance predictions for the Orion formation flying mission. *International symposium on formation flying: Missions and technologies*. 2002.

[19] D. Fernandez, F. Barcelo-Arroyo, I. Martin-Escalona, M. Ciurana, M. Jofre and E. Gutierrez. Fusion of WLAN and GNSS observables for positioning in urban areas: The position ambiguity. *2011 IEEE Symposium on Computers and Communications (ISCC)*. IEEE. 2011, 748–751.

[20] M. G. Fernández, Y. Á. López, A. A. Arboleya, B. G. Valdés, Y. R. Vaqueiro, F. L.-H. Andrés and A. P. García. Synthetic aperture radar imaging system for landmine detection using a ground penetrating radar on board a unmanned aerial vehicle. *IEEE Access* 6 (2018), 45100–45112.

[21] O. Frey, C. Magnard, M. Ruegg and E. Meier. Focusing of airborne synthetic aperture radar data from highly nonlinear flight tracks. *IEEE Transactions on Geoscience and Remote Sensing* 47.6 (2009), 1844–1858.

[22] H. T. Friis. A Note on a Simple Transmission Formula. *Proceedings of the IRE* 34.5 (May 1946), 254–256. ISSN: 0096-8390. DOI: 10.1109/JRPROC.1946.234568.

[23] N. Gebert. Multi-channel azimuth processing for high-resolution wide-swath SAR imaging. (2009).

[24] L. C. Godara. Applications of antenna arrays to mobile communications. I. Performance improvement, feasibility, and system considerations. *Proceedings of the IEEE* 85.7 (1997), 1031–1060.

[25] T. R. Godbole, M. Calvo-Fullana, A. Pyattaev, D. Mox, S. Andreev, A. Ribeiro and M. Valkama. Modeling mmWave Channels in High-Fidelity Simulations of Unmanned Aerial Systems. *2019 IEEE 20th International Workshop on Signal Processing Advances in Wireless Communications (SPAWC) (IEEE SPAWC 2019)*. Cannes, France, July 2019.

[26] N. Goddemeier and C. Wietfeld. Investigation of air-to-air channel characteristics and a UAV specific extension to the rice model. *2015 IEEE Globecom Workshops (GC Wkshps)*. IEEE. 2015, 1–5.

[27] L. Gupta, R. Jain and G. Vaszkun. Survey of important issues in UAV communication networks. *IEEE Communications Surveys & Tutorials* 18.2 (2016), 1123–1152.

[28] A. Harvey and R. Appleby. Passive mm-wave imaging from UAVs using aperture synthesis. *The Aeronautical Journal* 107.1069 (2003), 87–97.

[29] S. Hayat, E. Yanmaz and R. Muzaffar. Survey on unmanned aerial vehicle networks for civil applications: A communications viewpoint. *IEEE Communications Surveys & Tutorials* 18.4 (2016), 2624–2661.

[30] R. W. Heath, N. Gonzalez-Prelcic, S. Rangan, W. Roh and A. M. Sayeed. An overview of signal processing techniques for millimeter wave MIMO systems. *IEEE journal of selected topics in signal processing* 10.3 (2016), 436–453.

[31] A. Herique, W. Kofman, P. Bauer, F. Remy and L. Phalippou. A spaceborne ground penetrating radar: MIMOSA. *IEEE 1999 International Geoscience and Remote Sensing Symposium. IGARSS'99 (Cat. No. 99CH36293)*. Vol. 1. IEEE. 1999, 473–475.

[32] B. K. Horn. *Indoor positioning using time of flight with respect to WiFi access points*. URL: http://people.csail.mit.edu/bkph/ftmrtt_errors (visited on 06/10/2019).

[33] A. Hornung, K. M. Wurm, M. Bennewitz, C. Stachniss and W. Burgard. OctoMap: An efficient probabilistic 3D mapping framework based on octrees. *Autonomous robots* 34.3 (2013), 189–206.

[34] M. Ibrahim, H. Liu, M. Jawahar, V. Nguyen, M. Gruteser, R. Howard, B. Yu and F. Bai. Verification: Accuracy evaluation of WiFi fine time measurements on an open platform. *Proceedings of the 24th Annual International Conference on Mobile Computing and Networking*. ACM. 2018, 417–427.

[35] IEEE Standard for Information technology—Telecommunications and information exchange between systems Local and metropolitan area networks—Specific requirements - Part 11: Wireless LAN Medium Access Control (MAC) and Physical Layer (PHY) Specifications. *IEEE Std 802.11-2016 (Revision of IEEE Std 802.11-2012)* (Dec. 2016), 1–3534. DOI: 10.1109/IEEESTD.2016.7786995.

[36] M. T. Ivrlač and J. A. Nossek. The maximum achievable array gain under physical transmit power constraint. *2008 International Symposium on Information Theory and Its Applications*. IEEE. 2008, 1–6.

[37] M. T. Ivrlač and J. A. Nossek. High-efficiency super-gain antenna arrays. *2010 International ITG Workshop on Smart Antennas (WSA)*. IEEE. 2010, 369–374.

[38] S.-S. Jan and P. Enge. Using GPS to synthesize a large antenna aperture when the elements are mobile. *Proceedings of the National Technical Meeting of The Institute of Navigation*. 2000.

[39] R. L. Jordan. The Seasat-A synthetic aperture radar system. *IEEE Journal of Oceanic Engineering* 5.2 (1980), 154–164.

[40] A. A. Khuwaja, Y. Chen, N. Zhao, M.-S. Alouini and P. Dobbins. A survey of channel modeling for UAV communications. *IEEE Communications Surveys & Tutorials* 20.4 (2018), 2804–2821.

[41] D. M. Le Vine. The sensitivity of synthetic aperture radiometers for remote sensing applications from space. *Radio Science* 25.04 (1990), 441–453.

[42] D. M. Le Vine. Synthetic aperture radiometer systems. *IEEE Transactions on Microwave Theory and Techniques* 47.12 (1999), 2228–2236.

[43] D. M. Le Vine, T. T. Wilheit, R. E. Murphy and C. T. Swift. A multifrequency microwave radiometer of the future. *IEEE Transactions on Geoscience and Remote Sensing* 27.2 (1989), 193–199.

[44] D. Le Vine, A. J. Griffis, C. T. Swift and T. J. Jackson. ESTAR: A synthetic aperture microwave radiometer for remote sensing applications. *Proceedings of the IEEE* 82.12 (1994), 1787–1801.

[45] B. Li, Z. Fei and Y. Zhang. UAV Communications for 5G and Beyond: Recent Advances and Future Trends. *IEEE Internet of Things Journal* (2018).

[46] C. J. Li and H. Ling. Synthetic aperture radar imaging using a small consumer drone. *2015 IEEE international symposium on antennas and propagation & USNC/URSI national radio science meeting*. IEEE. 2015, 685–686.

[47] G. Lui, T. Gallagher, B. Li, A. G. Dempster and C. Rizos. Differences in RSSI readings made by different Wi-Fi chipsets: A limitation of WLAN localization. *2011 International Conference on Localization and GNSS (ICL-GNSS)*. IEEE. 2011, 53–57.

[48] A. Maltsev, A. Pudeyev, A. Lomayev and I. Bolotin. *Channel Models for IEEE 802.11ay, IEEE 802.11-15/1150r9*. IEEE 802.11-15/1150r9. IEEE. 2016.

[49] T. A. Milligan. *Modern antenna design*. Wiley Online Library, 2005.

[50] M. Mozaffari, W. Saad, M. Bennis and M. Debbah. Unmanned aerial vehicle with underlaid device-to-device communications: Performance and tradeoffs. *IEEE Transactions on Wireless Communications* 15.6 (2016), 3949–3963.

[51] K. Nur, S. Feng, C. Ling and W. Ochieng. Integration of GPS with a WiFi high accuracy ranging functionality. *Geo-spatial Information Science* 16.3 (2013), 155–168.

[52] J. Petko and D. Werner. Positional tolerance analysis and error correction of micro-UAV swarm based antenna arrays. *2009 IEEE Antennas and Propagation Society International Symposium*. IEEE. 2009, 1–4.

[53] V. Petrov, G. Fodor, J. Kokkoniemi, D. Moltchanov, J. Lehtomaki, S. Andreev, Y. Koucheryavy, M. Juntti and M. Valkama. On Unified Vehicular Communications and Radar Sensing in Millimeter-Wave and Low Terahertz Bands. *IEEE Wireless Communications* (2019).

[54] J. Pokorny, A. Ometov, P. Pascual, C. Baquero, P. Masek, A. Pyattaev, A. Garcia, C. Castillo, S. Andreev, J. Hosek et al. Concept design and performance evaluation of UAV-based backhaul link with antenna steering. *Journal of Communications and Networks* 20.5 (2018), 473–483.

[55] A. Pyattaev, K. Johnsson, S. Andreev and Y. Koucheryavy. A Novel Stochastic Channel Modeling Approach for mmWave Systems with Beamforming. *2016 IEEE 83rd Vehicular Technology Conference (VTC Spring)*. IEEE. 2016, 1–5.

[56] J. Rodriguez-Fernandez, N. Gonzalez-Prelcic and R. W. Heath. Position-Aided Compressive Channel Estimation and Tracking for Millimeter Wave Multi-User MIMO

Air-to-Air Communications. *2018 IEEE International Conference on Communications Workshops (ICC Workshops)*. IEEE. 2018, 1–6.

[57] J. Sánchez-García, J. García-Campos, M. Arzamendia, D. Reina, S. Toral and D. Gregor. A survey on unmanned aerial and aquatic vehicle multi-hop networks: Wireless communications, evaluation tools and applications. *Computer Communications* 119 (2018), 43–65.

[58] R. M. Sandoval, A.-J. Garcia-Sanchez and J. Garcia-Haro. Improving RSSI-based path-loss models accuracy for critical infrastructures: A smart grid substation case-study. *IEEE Transactions on Industrial Informatics* 14.5 (2017), 2230–2240.

[59] Y. Sato, H. Sawada and S. Kato. High gain beam-forming antenna with two-layer super gain antennas for 2.4 GHz wireless LAN. *2012 Asia Pacific Microwave Conference Proceedings*. IEEE. 2012, 1091–1093.

[60] M. Schartel, R. Burr, W. Mayer, N. Docci and C. Waldschmidt. UAV-based ground penetrating synthetic aperture radar. *2018 IEEE MTT-S International Conference on Microwaves for Intelligent Mobility (ICMIM)*. IEEE. 2018, 1–4.

[61] J. Stiles, N. Goodman and S. Lin. Performance and processing of SAR satellite clusters. *IGARSS 2000. IEEE 2000 International Geoscience and Remote Sensing Symposium. Taking the Pulse of the Planet: The Role of Remote Sensing in Managing the Environment. Proceedings (Cat. No. 00CH37120)*. Vol. 2. IEEE. 2000, 883–885.

[62] W. L. Stutzman. Estimating directivity and gain of antennas. *IEEE Antennas and Propagation Magazine* 40.4 (1998), 7–11.

[63] W. L. Stutzman and G. A. Thiele. *Antenna theory and design*. John Wiley & Sons, 2012.

[64] *Synthetic Aperture Radar (SAR)*. URL: https://www.dlr.de/dlr/en/desktopdefault.aspx/tabid-10382/ (visited on 06/10/2019).

[65] A. R. Thompson, J. M. Moran, G. W. Swenson et al. *Interferometry and synthesis in radio astronomy*. Wiley New York et al., 1986.

[66] S. Tonetti, M. Hehn, S. Lupashin and R. D'Andrea. Distributed control of antenna array with formation of UAVs. *IFAC Proceedings Volumes* 44.1 (2011), 7848–7853.

[67] B. D. Van Veen and K. M. Buckley. Beamforming: A versatile approach to spatial filtering. *IEEE ASSP magazine* 5.2 (1988), 4–24.

[68] H. J. Visser. *Array and phased array antenna basics*. Wiley Online Library, 2005.

[69] *Wi-Fi RTT (IEEE 802.11mc) | Android Open Source Project*. URL: https://source.android.com/devices/tech/connect/wifi-rtt (visited on 06/10/2019).

[70] C. A. Wiley. Synthetic aperture radars. *IEEE Transactions on Aerospace and Electronic Systems* 3 (1985), 440–443.

[71] Z. Xiao, P. Xia and X.-G. Xia. Enabling UAV cellular with millimeter-wave communication: Potentials and approaches. *IEEE Communications Magazine* 54.5 (2016), 66–73.

[72] J. Yan, Z. Peng, H. Hong, X. Zhu, Q. Lu, B. Ren and C. Li. Indoor range-direction-movement SAR for drone-based radar systems. *2017 IEEE Asia Pacific Microwave Conference (APMC)*. IEEE. 2017, 1290–1293.

[73] Y. Yu, R. Chen, L. Chen, G. Guo, F. Ye and Z. Liu. A Robust Dead Reckoning Algorithm Based on Wi-Fi FTM and Multiple Sensors. *Remote Sensing* 11.5 (2019), 504.

[74] H. Zhong and X. Liu. A New Combination Technique for Improving Slant Resolution in Constellation SAR System. *2006 IEEE International Symposium on Geoscience and Remote Sensing*. IEEE. 2006, 3152–3155.